



This discussion paper is/has been under review for the journal Atmospheric Measurement Techniques (AMT). Please refer to the corresponding final paper in AMT if available.

Big grains go far: reconciling tephrochronology with atmospheric measurements of volcanic ash

J. A. Stevenson¹, S. C. Millington², F. M. Beckett², G. T. Swindles³, and T. Thordarson⁴

¹School of GeoSciences, University of Edinburgh, Edinburgh, UK

²Met Office, Exeter, UK

³School of Geography, University of Leeds, Leeds, UK

⁴Institute of Earth Sciences, Háskóli Íslands, Reykjavík, Iceland

Received: 31 October 2014 – Accepted: 2 December 2014 – Published: 6 January 2015

Correspondence to: J. A. Stevenson (john.stevenson@ed.ac.uk)

Published by Copernicus Publications on behalf of the European Geosciences Union.

Big grains go far

J. A. Stevenson et al.

Title Page

Abstract

Introduction

Conclusions

References

Tables

Figures



Back

Close

Full Screen / Esc

Printer-friendly Version

Interactive Discussion



Abstract

There is a large discrepancy between the size of volcanic ash particles measured from deposits on the ground (known as cryptotephra; 20–125 μm in length) and those reported by satellite remote sensing (effective radii of 0.5–9 μm ; 95 % of particles < 17 μm diameter). We use results from the fields of tephrochronology (a dating technique based on volcanic ash layers), dispersion modelling and satellite remote sensing in an attempt to understand from where it arises. We show that Icelandic cryptotephra deposited in NW Europe have lognormal particle size distributions (PSDs) with median lengths of 20–70 μm (geometric standard deviation: 1.40–1.66; 95th percentile length: 42–126 microns). This is consistent with semi-quantitative grainsize range estimates from the literature. Using measured fall velocities of ash particles, a release height typical of moderate Icelandic eruptions (10 km) and a wind speed typical for NW Europe (10 ms^{-1}), we find that an ash cloud can transport particles < 80 μm diameter up to 850 km in 24 h, so that even moderately sized Icelandic eruptions can deposit cryptotephra on mainland Europe. The proportion of cryptotephra in airborne clouds is unknown. We used simulated satellite data of dispersion-model-derived ash clouds to investigate the effect of PSD on satellite retrievals and show that as the median radius of the input PSD increases, fewer ash-containing pixels are correctly identified. Where retrievals are made of simulated clouds with mass median radii larger than $\sim 10 \mu\text{m}$, the mean retrieved r_{eff} plateaus at around 9 μm . This is a systematic bias in the retrieval algorithm that would cause the grainsize of distal clouds containing significant cryptotephra to be underestimated. This cannot explain discrepancies in coarser proximal clouds, however, which may be because the complex physics of scattering by highly irregularly-shaped grains is inadequately represented by assuming that particles are dense spheres.

AMTD

8, 65–120, 2015

Big grains go far

J. A. Stevenson et al.

Title Page

Abstract

Introduction

Conclusions

References

Tables

Figures

◀

▶

◀

▶

Back

Close

Full Screen / Esc

Printer-friendly Version

Interactive Discussion



1 Introduction

Comparison of published distal volcanic ash grainsize data highlights striking differences between the fields of volcanology (tephrochronology), and dispersion modelling and satellite remote sensing. Differences in their approaches and frame of reference are highlighted by the terminology of each. In volcanology, “*coarse*” ash refers to particles 1–2 mm in diameter and those < 64 µm are classified as “*extremely fine*” (White and Houghton, 2006); in atmospheric science (dispersion models and satellite remote sensing), airborne particles coarser than 2 µm diameter are defined as “*coarse*” aerosol (Seinfeld and Pandis, 2006). Furthermore, volcanologists describe particle sizes via grain lengths, whereas atmospheric scientists use the particle radius. Tephrochronologists, who extract volcanic ash grains (known as cryptotephra) from soils or lakes hundreds of kilometers from their source, typically report grain lengths of 20–125 µm (Sect. 1.1). In contrast, measurements of airborne volcanic ash clouds by satellite remote sensing and direct sampling by aircraft find particle size distributions (PSDs) with median radii of 1–4 µm in which cryptotephra-sized grains form negligible proportions (Sect. 1.2). Assuming that the cryptotephra were transported to distal regions in volcanic ash cloud, their absence from measured ash cloud PSDs, particularly those close to the volcano (Sect. 1.3), is intriguing and is the focus of this study, which integrates new results from all three disciplines to investigate the size distributions of distal volcanic ash deposits, cryptotephra transport models and the influence of larger particles on satellite remote sensing results.

Our results highlight the importance of considering cryptotephra-sized grains in remote-sensing and atmospheric dispersion modelling and the need for empirical, quantitative measurements of the optical and aerodynamic properties of volcanic ash. They are presented in here in three sections: Sect. 2 covers cryptotephra size distributions, Sect. 3 covers transport models and Sect. 4 pertains to simulated satellite imagery. In each section, particle sizes are described using the dimension appropriate

AMTD

8, 65–120, 2015

Big grains go far

J. A. Stevenson et al.

Title Page

Abstract

Introduction

Conclusions

References

Tables

Figures



Back

Close

Full Screen / Esc

Printer-friendly Version

Interactive Discussion



ate to that field. These are length, diameter and radius, respectively. The findings are discussed in Sect. 5.

1.1 Generation, transport and deposition of cryptotephra

There is abundant evidence for distal (> 500 km) volcanic ash transport provided by grains preserved in soil (peat) and lake deposits, or in snow and glacial ice, which are identified by tephrochronologists (e.g. Persson, 1971; Dugmore, 1989; Abbott and Davies, 2012). Geochemical analyses by electron probe microanalysis (EPMA) or secondary ion mass spectrometry (SIMS) can link cryptotephra to their source volcano and possibly an eruption of known age, making tephrochronology a powerful dating tool (Swindles et al., 2010; Hayward, 2012). Very distal deposits are too thin to form a visible layer, but ash grains can be extracted in the laboratory (Hall and Pilcher, 2002; Swindles et al., 2010). These “cryptotephra” grains (also called “microtephra” or glass “shards”) are recognised by their glassy colour (\pm the presence of crystals), their highly irregular shapes and their often vesicular texture (Dugmore, 1989; Lowe, 2011). Their size is described by their *long axis length*, defined as the longest distance between two parallel tangents across the grain, which typically ranges from 20 to > 125 μm . Unfortunately, grainsizes are not routinely reported, and when they are the data are often just exemplar, modal or maximum lengths. More quantitative descriptions of the size distribution could be used to inform dispersion modelling in the far field.

Cryptotephra-sized grains are transported to distal regions in ash clouds whose initial PSD depends on the characteristics of the eruptions that produce them. Particles can range in size over 7 orders of magnitude from microns to metres in diameter. The PSD of all ejected particles is known as the Total Deposit Grainsize Distribution (TGSD; Bonadonna and Houghton, 2005; Rust and Cashman, 2011). The TGSD varies significantly between eruptions and is strongly controlled by the size distribution of bubbles in the magma, which depends on the magma composition (basaltic eruptions have coarser products than rhyolitic ones), gas content, particle collisions, ascent rate and external factors such as interaction with water (Rose and Durant, 2009). The propor-

Big grains go far

J. A. Stevenson et al.

Title Page

Abstract

Introduction

Conclusions

References

Tables

Figures



Back

Close

Full Screen / Esc

Printer-friendly Version

Interactive Discussion



tion of cryptotephra-sized grains is larger than that of the finest particles that are most easily identified in remote sensing data. Even in rhyolite eruptions, only around 1/3 of ejected material is finer than 12 μm diameter (Rust and Cashman, 2011) and therefore BTD-active.

The PSD evolves during transport as particles fall out of the plume. The terminal velocity of volcanic ash particles (typically 0.15–0.35 ms^{-1} for grains around 100 μm in length; Riley et al., 2003) is much less than a sphere of the same diameter; a 100 μm grain may fall at the same rate as a sphere 9–50 μm in diameter (Rose et al., 2003). PSDs of deposits show that particles > 500 μm are mostly deposited within tens of kilometres of the volcano (Rose et al., 2001). At distances up to 500 km, deposits contain a significant proportion of ash particles (< 100 μm) that are deposited much earlier than would be predicted by single particle settling velocities. In proximal areas, vertical gravity currents (similar to microbursts) can transport particles to the ground faster than their individual terminal velocities as streak fallout (Eliasson et al., 2014). Aggregation and meteorological processes such as coating of ash particles by ice or water and subsidence of the entire volcanic plume may also be important in the distal evolution of the PSD (Durant et al., 2009). Satellite retrievals of ash cloud mass indicate that after ~ 24 h, just a small proportion (< 5%) of the erupted mass remains in the cloud to be transported to distal locations (Rose et al., 2000, 2001; Gudmundsson et al., 2012). Comparisons of Numerical Atmospheric-dispersion Modelling Environment (NAME) dispersion model predictions with measurements from aircraft (Dacre et al., 2013) and ground-based LiDAR (Devenish et al., 2012) during the 2010 Eyjafjallajökull eruption found similar proportions (2–6 and 2–12 %, respectively).

1.2 Satellite detection of volcanic ash

Satellite remote sensing distinguishes volcanic ash clouds from meteorological clouds using the different optical properties of ash and water or ice droplets (Prata, 1989; Wen and Rose, 1994). Infrared energy radiated upwards from the earth's surface is absorbed and scattered by ash, water and ice particles (as well as other aerosols) and this

Big grains go far

J. A. Stevenson et al.

Title Page

Abstract

Introduction

Conclusions

References

Tables

Figures

◀

▶

◀

▶

Back

Close

Full Screen / Esc

Printer-friendly Version

Interactive Discussion



Big grains go far

J. A. Stevenson et al.

Title Page

Abstract

Introduction

Conclusions

References

Tables

Figures

◀

▶

◀

▶

Back

Close

Full Screen / Esc

Printer-friendly Version

Interactive Discussion



affects the brightness temperature measured by a satellite instrument for a given pixel. The brightness temperature difference (BTD) of a pixel between two infrared channels centred at 10.8 and 12.0 μm is often used to identify ash clouds (this is sometimes also referred to as the reverse-absorption or split-window method). Volcanic ash is more absorbing at 10.8 μm than at 12.0 μm and gives a negative BTD, whilst water and ice clouds have the opposite characteristics. The strength of absorption and scattering by particles is a function of the wavelength, particle size, particle shape and the complex refractive indices of the volcanic glass from which it is formed. Mie theory models these interactions by assuming spherical particles and is applicable where the the particles are of a similar size to the wavelength of the radiation, thus it is important to take account of the particle size distribution (PSD) when using the BTD technique. Coarser particles will not have a differential absorption effect resulting in similar brightness temperatures at 10.8 and 12.0 μm . Ash clouds dominated by such coarse particles are optically opaque at high concentrations (Rose et al., 2001) and, although they may be recognised by skilled human operators, automatic detection using the BTD method is not possible. Particle shape and composition are also important (Pollack et al., 1973; Wen and Rose, 1994; Kylling et al., 2014). More sophisticated ash detection algorithms use extra tests to reduce false positives or negatives, or take volcanic SO_2 into account, by incorporating data from a third infrared channel (Francis et al., 2012; Pavolonis et al., 2013) or even many channels of hyperspectral data (Gangale et al., 2010), but these also rely on size-dependant scattering of infrared radiation by ash particles to some extent.

Once a pixel has been identified as ash-contaminated, ash cloud properties such as height, ash column loading and particle effective radius (r_{eff} , which is a function of the PSD – see Appendix; Wen and Rose, 1994; Prata and Prata, 2012; Francis et al., 2012; Pavolonis et al., 2013), can be retrieved. Mie theory allows the absorption and scattering coefficients for a given r_{eff} , refractive index (ash composition) and wavelength to be predicted, based on the assumption that the particles are dense spheres. Assuming a thin, homogeneous, semi-transparent, surface-parallel cloud, a radiative transfer

Big grains go far

J. A. Stevenson et al.

Title Page

Abstract

Introduction

Conclusions

References

Tables

Figures



Back

Close

Full Screen / Esc

Printer-friendly Version

Interactive Discussion



model can be used to calculate the BTD for different PSDs (expressed in terms of their effective radius, r_{eff}) and ash mass loading (a function of optical depth, τ_c) for a range of cloud heights and meteorological conditions (Wen and Rose, 1994). Some retrieval methods also assume a fixed ash cloud altitude (Wen and Rose, 1994; Prata and Prata, 2012). Retrieval algorithms attempt to find the combination of parameters that best produce the observed brightness temperatures in a satellite image (Wen and Rose, 1994; Prata and Prata, 2012; Francis et al., 2012; Pavolonis et al., 2013).

Each retrieved r_{eff} represents a PSD containing a narrow range of particle sizes. It has been acknowledged since the BTD method was developed that it requires ash clouds dominated by particles $< 10 \mu\text{m}$ diameter, which corresponds to PSDs with an effective radius less than $\sim 17 \mu\text{m}$ (Prata, 1989; Wen and Rose, 1994). A lognormal distribution with a geometric standard deviation, σ of 2.0, and an effective radius of $17 \mu\text{m}$ has 95 % of particles $< 32 \mu\text{m}$ diameter, with 95 % of the mass within particles $< 135 \mu\text{m}$ (see Fig. 1 and Appendix). These distributions therefore contain significant proportions of cryptotephra-sized particles. Published values of retrieved r_{eff} , however, are never this high, and range from 0.5 to $9 \mu\text{m}$ (Grainger et al., 2013). Such distributions have 95 % of particles less than 0.9 to $17 \mu\text{m}$ in diameter, respectively, with 95 % of the mass within particles less than 4 or $72 \mu\text{m}$. These PSDs suggest that the proportion of cryptotephra-sized particles within ash clouds is small to negligible.

1.3 Comparing remote sensing PSDs with proximal deposits

In a few cases, satellite retrievals have been made of proximal volcanic ash clouds where samples have also been taken from the ground. The PSDs of the deposits contain significant cryptotephra-sized (and coarser) grains, yet the retrieved PSDs suggest that these formed a negligible proportion of the depositing ash cloud. For example, the deposits of the 1996 eruption of Ruapehu, New Zealand are exceptionally well characterised (Bonadonna and Houghton, 2005). The total grainsize distribution of material deposited on land between 50 and 200 km from the volcano has a mode of $125 \mu\text{m}$, with $> \sim 80 \%$ of deposited mass made up of grains coarser than $64 \mu\text{m}$. This com-

pares to effective radius estimates derived from AVHRR-2 and ATSR-2 data of 2–4 μm in the same region (Prata and Grant, 2001), which would imply that 95% of the mass is within grains with a diameter of less than 16–32 μm .

More recently, SEVIRI retrievals were compared with ground-based sampling during the 2010 Eyjafjallajökull summit eruption (Bonadonna et al., 2011). Samples collected on the ground 56 km downwind from the volcano on 6 May 2010 contained grains 1–500 μm in diameter, with a mode of 64 μm and were deposited at a sedimentation rate of $0.4 \times 10^{-4} \text{ kg m}^{-2} \text{ s}^{-1}$. The nearest available satellite retrieval for the same day was at a location 130 km downwind of the crater. The mean retrieved ash radius was 4 μm corresponding to a sedimentation rate of $0.2\text{--}0.4 \times 10^{-6} \text{ kg m}^{-2} \text{ s}^{-1}$, which is over 100 \times less. It was suggested that the 2-orders-of-magnitude discrepancy over 50 km range is a “consequence of ash aggregation and convective instabilities”. Bonadonna et al. (2011) also note that there are limits on the detection of ash particles due to their size, which only allow for the retrieval of particles with diameters of $< 20 \mu\text{m}$.

Taking the Eyjafjallajökull 2010 summit eruption as a whole, Stohl et al. (2011) used SEVIRI data to inform the inversion of a Lagrangian particle dispersion model, and estimated the total mass of ash of 2.8–28 μm diameter emitted over the entire duration of the eruption was $8.3 \pm 4.2 \text{ Tg}$. They included a secondary mode of coarser particles in the input size distribution (modal size = 180 μm) in order to match the measured size distributions on the ground. Their estimated erupted mass is nearly an order-of-magnitude lower than the 70 Tg of particles finer than 28 μm calculated by mapping the thickness, mass and grainsize distribution of tephra on the ground (Gudmundsson et al., 2012).

Comparing proximal deposits with satellite retrievals shows a large discrepancy in PSDs. Here we suggest that distal deposits are likely to have the same issue and suggest that it may result, in part, from the lack of sensitivity of the detection and retrieval methods to large particles and to the assumption of spherical particles used in the calculation of the extinction coefficients.

Big grains go far

J. A. Stevenson et al.

Title Page

Abstract

Introduction

Conclusions

References

Tables

Figures

◀

▶

◀

▶

Back

Close

Full Screen / Esc

Printer-friendly Version

Interactive Discussion



used for the wavelength-dispersive spectroscopy (WDS) analyses. At Leeds a Jeol 8230 electron microprobe with an equivalent setup was used. Microprobes were calibrated using both natural and synthetic standards and instrument stability was monitored using a range of glass standards. Tephabase (Newton et al., 2007) was used to identify the tephtras.

2.2 Results

2.2.1 Literature examples of cryptotephra grainsizes

Literature data from a range of sources are summarised in Table 1. They are dominated by single measurements of modal or maximum size. The work of Persson (1971) is a notable exception, and those data have been digitized and included here. Published sizes range from 10–150 μm , with values from 30–60 μm being common.

The deposition of Icelandic cryptotephtras in Europe is well-characterised, with 19 cryptotephtras from the past 1000 years identified to date (Swindles et al., 2011). Small eruptions such as Eyjafjallajökull 2010, Grímsvötn 2011 and Hekla 1510 deposited grains up to 110, 80 and 70 μm respectively in the UK (800–1500 km from source; Stevenson et al., 2012, 2013; Dugmore et al., 1996). The most widespread layers (i.e. the Vedde ash) can be identified in Russia and Slovenia, over 2500 km from source (Lane et al., 2012). Some of the world's largest eruptions such as the Taupo Whakamaru eruption (New Zealand), the Toba Younger Toba Tuff eruption (Indonesia) and the Campanian Ignimbrite (Italy), deposited ash layers 2–10 cm thick containing significant quantities of grains $> 64 \mu\text{m}$ at distances of > 1000 km from their source (Matthews et al., 2012; Engwell et al., 2013). Such large eruptions, with Volcano Explosivity Index (VEI) scores of 7 or 8, are rare (recurrence intervals of > 1000 and $> 10\,000$ years, respectively; Newhall and Self, 1982). However, the correlation of the White River Ash (Alaska, 50 km³ tephra) with the AD860 tephra in Greenland and Europe (7000 km range) shows that even eruptions of a size that occurs around once-per-century are capable of generating ultradistal cryptotephtra (Jensen et al., 2014).

Title Page

Abstract

Introduction

Conclusions

References

Tables

Figures



Back

Close

Full Screen / Esc

Printer-friendly Version

Interactive Discussion



Big grains go far

J. A. Stevenson et al.

Title Page

Abstract

Introduction

Conclusions

References

Tables

Figures

◀

▶

◀

▶

Back

Close

Full Screen / Esc

Printer-friendly Version

Interactive Discussion



Ice cores provide an excellent record of distal cryptotephra as they are less contaminated by mineral grains and because peaks in sulphate concentration can be used to locate ash layers (Abbott and Davies, 2012), thus smaller grains ($< 5 \mu\text{m}$) from extremely distal events can also be identified. Ice core grain size and distance data are also summarised in Table 1, and provide further evidence for transport of cryptotephra-sized grains to distances $> 500\text{--}1000 \text{ km}$ from the source volcano. Icelandic volcanoes were the source of 37 of 45 cryptotephra identified in Greenland ice cores (Abbott and Davies, 2012). All layers, most of which were invisible to the naked eye, contained grains $> 30 \mu\text{m}$ and many had grains $> 60 \mu\text{m}$ diameter. The shortest distance from Iceland's most active volcanoes to the Greenland core sites is $\sim 1500 \text{ km}$, but given the prevalence of westerly winds, it is likely that many of these arrived via a much longer, circumpolar route (Mortensen et al., 2005). Cryptotephra grains from volcanoes in the USA (Mount Mazama, Aniakchak, Katmai) and Mexico (El Chichón) are also found. In Antarctica, ice cores (e.g. Dome C, Siple Dome) also yield ash grains; those with different chemistry to local sources (e.g. Antarctic volcanoes, Deception Island, Taupo) are attributed to much more distant (6000 km) eruptions (i.e. Andean volcanoes; De Angelis et al., 1985). In the case of the 1257 eruption of Samalas volcano, Indonesia (Lavigne et al., 2013), tephra shards $< 5 \mu\text{m}$ long with matching compositions have been found at both the GISP2 site in Greenland and the South Pole site in Antarctica (Palais et al., 1992), implying a transportation range of $13\,500 \text{ km}$.

2.2.2 Measured grain size distributions of Icelandic cryptotephra

Grain size distribution curves are compared in Fig. 2a, while the measured data and fitted curves are shown in Fig. 3 and in the Supplement. Their statistics are summarised in Table 2. The PSDs for the cryptotephra recovered from peat are best described ($r^2 > 98\%$) by lognormal distributions with number median lengths of $48\text{--}70 \mu\text{m}$ and geometric standard deviation (σ) of $1.40\text{--}1.55$, corresponding to 95% of particles less than $42\text{--}126 \mu\text{m}$ long. The PSDs of Grímsvötn 2011 cryptotephra were finer (median lengths $19\text{--}23 \mu\text{m}$). The lognormal distribution implies that assuming a normal distribu-

Big grains go far

J. A. Stevenson et al.

Title Page

Abstract

Introduction

Conclusions

References

Tables

Figures



Back

Close

Full Screen / Esc

Printer-friendly Version

Interactive Discussion



tion and reporting mean and standard deviation underestimates the relative importance of fine grains as well as the maximum likely grain size. The distributions are narrower than those obtained through airborne sampling of distal ash clouds ($\sigma = 1.8\text{--}2.5$; Johnson et al., 2012) and contain a negligible proportion ($\ll 1\%$) of grains $< 12\ \mu\text{m}$ long (that would produce a BTM effect). The particles are vesicular and extremely irregular in shape (Fig. 4), as is typical for cryptotephra. This also makes it difficult to convert a number distribution into a mass distribution.

Samples from the Askja 1875 and Eyjafjallajökull 2010 eruptions, collected in Sweden (12.25°E , 61.33°N) and the Faroe Islands (-6.79°E , 62.01°N), respectively, contained sufficient material for Coulter Counter laser diffraction particle size analysis, which is sensitive to particles down to $0.4\ \mu\text{m}$. It records a particle volume distribution based on the equivalent area diameter, defined as the diameter of a sphere with the same cross-sectional area as the particle. The equivalent area diameter is smaller than the long axis length (Riley et al., 2003). The PSDs (Fig. 2b) are best described by Weibull distributions, with a shape of $1.37\text{--}1.48$ and a scale of $40\text{--}55\ \mu\text{m}$. This form of PSD has been linked to the sequential fragmentation/transport model of tephra grain-size evolution (Wohletz et al., 1989) and may be typical of laser diffraction data. Distal Campanian Ignimbrite deposits (Engwell et al., 2013) are also well described by Weibull distributions (shape $0.95\text{--}1.22$, scale: $58\text{--}72$). The Weibull distribution has a fine tail compared to the lognormal distribution. It is possible that such particles were missed by the microscope counting method. However, Fig. 2 shows that BTM-active particles with diameters $< 12\ \mu\text{m}$ represent only a small proportion of grains, indicating that the microscope counting method correctly captures the peak of the cryptotephra size distribution.

The cryptotephra size distributions presented here are number distributions in terms of grain length. Due to the vesicular and extremely irregular shape of the grains, it is not appropriate to assume that they are dense spheres when converting to a mass distribution. One possible approach is to convert the median grain lengths into median equivalent volume diameters using the ratios calculated by Riley et al. (2003) for dif-

ferent compositions. These range from 1.05–1.17 for basalt and 1.14–1.33 for rhyolite. Results of this are shown in Table 3. Without specific information on particle shape and vesicularity, it is not possible to determine the correct ratio, and these numbers are reported to illustrate that the bulk of the mass of the size distribution is within the larger particles.

Figure 5 shows the variation in grainsize of Icelandic cryptotephra in Europe with distance from the source volcano. There is significant scatter in the tephrochronological data, which represents particles from different eruptions with different meteorological conditions. Few cryptotephra are finer than 20 μm . There is very poor correlation between diameter and transport distance. The UK-deposited cryptotephtras from the 2011 Grímsvötn eruption, which were transported from the lowest 4 km of the eruption plume are notable for their small grainsize (Stevenson et al., 2013). With the exception of Hekla 1947, UK cryptotephtras from Hekla are rhyolite in composition and are characterised by relatively large grainsizes (95th percentile grain diameters of 82–125 μm). The coarsest distal examples from the literature correspond to the Saksunarvatn and Vedde Ash tephtras, which are characterised by bubble-wall shaped shards of thin volcanic glass (Lane et al., 2011; Housley et al., 2013).

3 Model constraints on cryptotephra transport

3.1 Method

We carried out simple transport modelling to determine the terminal velocity and transport range of cryptotephra particles, which depend on the size, density and shape of the particle, and on atmospheric conditions (including the wind velocity) and the release height. The aim was to investigate the size of ash grains capable of being deposited in Europe following a moderately sized Icelandic eruption. We used two different schemes to calculate particle terminal fall velocity. The simplest possible scheme uses Stokes' settling law and assumes spherical particles with a density of 2300 kg m^{-3} (rhyolitic

Title Page

Abstract

Introduction

Conclusions

References

Tables

Figures



Back

Close

Full Screen / Esc

Printer-friendly Version

Interactive Discussion



Big grains go far

J. A. Stevenson et al.

Title Page

Abstract

Introduction

Conclusions

References

Tables

Figures



Back

Close

Full Screen / Esc

Printer-friendly Version

Interactive Discussion



glass) falling in a constant atmosphere. A more realistic analysis accounts for the non-spherical shape of the particles by using a Reynolds number dependent drag coefficient (Ganser, 1993) that varies with the sphericity (Ψ_R) of the particle (see Appendix B) for details). $\Psi_R = 0.7$ was chosen for the Ganser scheme based on values from Riley et al. (2003) for a rhyolitic (Ash Hollow member, Nebraska; $\Psi_R = 0.6$ – 0.8) composition. The variation in density with grain size was incorporated by using the relationship presented by Bonadonna and Phillips (2003), where the density decreases linearly from that of dense glass (2300 kg m^{-3} for Askja 1875) to that of pumice (440 kg m^{-3}) as size increases from $8 \mu\text{m}$ to 2 mm .

The more realistic analysis also uses a standard, stratified, atmosphere. In a standard atmosphere the atmospheric density and viscosity decrease upwards, causing the terminal velocity of the ash particles to increase with height above sea level. The atmospheric effect is minor compared to corrections for the sphericity and density distribution of the ash particles, which act to decrease settling velocity. The two schemes were compared to measured terminal fall velocities (at sea level) of ash particles given by Riley et al. (2003), who report data for basaltic, andesitic and rhyolite compositions as a function of dimensions such as long axis length and equivalent area diameter (Fig. 12). These dimensions correspond to the measurements made by tephrochronologists and optical particle size measuring equipment, respectively (Sect. 2.1).

A mean wind speed of 10 ms^{-1} was chosen based on NCEP re-analysis data of wind speeds over Iceland during the eruption of Eyjafjallajökull in spring 2010 (Petersen et al., 2012) and timings of contemporary reports of volcanic ash pollution in Europe following Icelandic eruptions (Askja 1875, Hekla 1947, Eyjafjallajökull 2010, Grímsvötn 2011; see Table 4). We used a release height of 10 km , the maximum plume height of the 2010 Eyjafjallajökull eruption, which is reasonable for a moderately-sized Icelandic eruption (Gudmundsson et al., 2012). Atmospheric turbulence, rising or subsiding air masses and particle aggregation are neglected in these simple treatments.

3.2 Results

Given a horizontal wind speed of 10 m s^{-1} , particles can be transported 850 km in 24 h . This is consistent with results of detailed climatological analysis that found that ash from a small Hekla eruption has a 15 % probability of reaching Scotland, Northern Ireland, Norway or Sweden within 24 h , but that transport as far as the Mediterranean was also possible in that time (Leadbetter and Hort, 2011). The formation of cryptotephra deposits also depends on how long the particles remain airborne. This was calculated using each of the particle terminal velocity schemes, along with the distance travelled in that time. The results are shown in Fig. 6 and summarised in Table 5.

All schemes predict that cryptotephra sized particles released by a moderately-sized Icelandic eruption can remain airborne for at least 24 h and can travel as far as the distance to London under reasonable wind conditions. The Stokes' and Ganser schemes give similar results, with the Ganser scheme predicting that particles can travel slightly further. Using the terminal velocity data for rhyolite particles results in a significant increase in the predicted travel distance of ash particles compared to the Stokes' and Ganser schemes. It corresponds to a $3\times$ increase over dense spheres for $50 \mu\text{m}$ equivalent area diameter particles (Fig. 6) These results show that in the absence of processes such as rainfall or aggregation, we should expect even moderately-sized Icelandic eruptions to deposit cryptotephra in mainland Europe. Ash Hollow data are presented both in terms of particle length and particle equivalent area diameter. For rhyolite, the particle length is $1.44\text{--}1.71\times$ the equivalent area diameter of the same particle (Riley et al., 2003). The measured terminal velocity of rhyolite particles was lower than basaltic particles, which fell at the same rate as rhyolite particles $1.18\text{--}1.68\times$ their equivalent area diameter. The uncertainties on measured Ash Hollow particle lengths for given terminal velocities are not known but are likely to be significant.

The calculated transport distances of particles are compatible with our cryptotephra grainsize distributions and with measurements of maximum grainsize by tephrochronologists (Fig. 6). Median cryptotephra transport distances from our results are generally

Title Page

Abstract

Introduction

Conclusions

References

Tables

Figures



Back

Close

Full Screen / Esc

Printer-friendly Version

Interactive Discussion



well represented by the calculated distances using the Stokes' or Ganser schemes, but calculations based on measured fall velocities are closer to maximum grainsize measurements and the coarsest literature values.

4 Satellite retrievals of cryptotephra-rich plumes

4.1 Method

We investigated how satellite retrievals of ash characteristics change as the particle size increases. We used a modelling approach based on simulated satellite imagery representing data from the Spinning Enhanced Visible and Infrared Imager (SEVIRI) instrument on the geostationary Meteosat satellite (Millington et al., 2012; Kylling et al., 2013). Consequently, the input parameters were known and could be controlled. As the assumptions used in generating the simulated images are the same as those used in the retrievals, this represents a validation of the retrieval algorithm itself and not the physics of the BTM technique. Mie theory was used to model the absorption and scattering coefficients for volcanic ash with different refractive indices and size distributions at different wavelengths of infrared. The refractive indices for andesite (Pollack et al., 1973) were used, in common with other studies (e.g. Pavolonis et al., 2006; Francis et al., 2012). Millington et al. (2012) quantified the effect of using the refractive indices of andesite, volcanic dust, obsidian and desert dust to simulate images of volcanic ash clouds. They found that data simulated using andesite and desert dust refractive indices gave the best agreement with measured satellite data for the 2010 Eyjafjallajökull eruption and the effect of varying refractive index on the simulated BTM was much smaller than that of changing the concentration or particle size distribution.

Radiative transfer calculations were performed using RTTOV-11, which is a very fast radiative transfer model for nadir viewing passive infrared and microwave satellite radiometers, spectrometers and interferometers (see Matricardi, 2005; Saunders et al., 2012, for details of the RTTOV-11 aerosol scattering and absorption scheme and val-

Title Page

Abstract

Introduction

Conclusions

References

Tables

Figures



Back

Close

Full Screen / Esc

Printer-friendly Version

Interactive Discussion



Big grains go far

J. A. Stevenson et al.

Title Page

Abstract

Introduction

Conclusions

References

Tables

Figures



Back

Close

Full Screen / Esc

Printer-friendly Version

Interactive Discussion



idation data). The inputs to RTTOV-11 were Numerical Atmospheric-dispersion Modelling Environment (NAME; Jones et al., 2006) simulations of a volcanic ash cloud and Numerical Prediction Weather (NWP) meteorological data from the Met Office's Global version of the Unified Model (Davies et al., 2005). RTTOV-11 was run without water and ice clouds in the simulations such that the ash cloud was simulated in a clear sky (surface and atmospheric water vapour and temperature variations were still present).

Simulations were performed using meteorological data and ash clouds modelled by NAME from the Eyjafjallajökull eruption for 12:00 UTC on the following dates: 14 and 15 April, 6, 7, 8, 9, 11, 13, 14, 15, 16 and 17 May. In each case, the location, altitude and concentration of volcanic ash predicted by NAME were used. The concentration data were converted to number density assuming the same lognormal PSD in all pixels and interpolated onto the NWP grid for modelling. The interpolation is necessary because the atmospheric dispersion model, NAME, is run at a finer resolution than the NWP model. In a real ash cloud the size distribution would vary downwind from the volcano as grains are deposited (Rose et al., 2001); this is a topic for future studies of simulated imagery. As the aim of this study was to compare a range of PSD and weather conditions, comparisons were made on a pixel-by-pixel basis and using a homogeneous cloud grainsize does not affect our conclusion. The geometric standard deviation of the PSD (σ) was fixed at 2.0, following Pavolonis et al. (2013) and in line with airborne measurements of the Eyjafjallajökull ash cloud ($\sigma = 1.8$ – 2.5 ; Turnbull et al., 2012; Johnson et al., 2012) and the mass median radius of the PSD was varied from 0.5–32 μm . The outputs are simulated brightness temperatures (BTs) for SEVIRI infrared channels. High concentrations of large particles cause ash clouds to become opaque (Rose et al., 2001). In the simulations presented here, the concentration of ash was sufficiently low for the clouds to be optically semi-transparent, even when dominated by larger particles.

Retrievals were made on the simulated images using the method of Francis et al. (2012). The primary test for volcanic ash uses the brightness temperature difference method; additional pixels may be detected by tests using data from the 8.7 μm chan-

Big grains go far

J. A. Stevenson et al.

Title Page

Abstract

Introduction

Conclusions

References

Tables

Figures



Back

Close

Full Screen / Esc

Printer-friendly Version

Interactive Discussion



nel and simulated clear-sky radiances, or removed by a test using the effective cloud emissivities and a spatial filtering test. Once ash-contaminated pixels have been identified, a retrieval of the physical properties is carried out using data from channels centred at 10.8, 12.0 and 13.4 μm to obtain estimates for the ash layer pressure (p_{ash} ; a proxy for the altitude of the cloud), the ash column mass loading (L), and the ash size distribution effective radius (r_{eff}). These values can then be compared to the original input values (see Fig. 8 for methodology flowchart). The retrievals are carried out using a one-dimensional variational (1D-Var) framework, which attempts to reach a statistically optimal estimate of the three physical properties of ash (p_{ash} , L , r_{eff}) consistent with the satellite data (real or simulated) and any prior background knowledge by minimising a cost function (Francis et al., 2012). This has the advantage that the total cost of the solution, which describes how closely the result matches the measured radiances and (weak) a priori constraints, can be used as a measure of uncertainty. The lower the total cost the lower the level of uncertainty in the retrievals.

4.2 Results

Initial modelling using Mie theory shows that, for SEVIRI, a negative BTM can only occur for individual (or monodisperse) spherical andesite particles (using refractive indices from Pollack et al., 1973) with diameters less than $\sim 12 \mu\text{m}$ and that the effect is strongest for particles with diameters $< 6 \mu\text{m}$ (Fig. 7). Only these particles contribute to the BTM effect. However, volcanic ash clouds contain particles with a range of sizes. Calculations using a lognormal PSD with geometric standard deviation (σ) of 2.0, show that a (weak) negative BTM is produced for distributions with mass median radius up to 21.5 μm . This corresponds to $r_{\text{eff}} = 16.5 \mu\text{m}$, which is in good agreement with Wen and Rose (1994).

Comparison between the input and the retrieved ash parameters for two example grainsize distributions (PSD mass median radius of 4 and 12 μm) as shown in Fig. 9a–c demonstrates the sensitivity of satellite identification of ash-containing pixels and retrievals to grainsize. In both cases, the retrieved effective radii are scattered across

Big grains go far

J. A. Stevenson et al.

Title Page

Abstract

Introduction

Conclusions

References

Tables

Figures

◀

▶

◀

▶

Back

Close

Full Screen / Esc

Printer-friendly Version

Interactive Discussion



a range of values ($\pm 3\text{--}8\ \mu\text{m}$ around the mean) due to variations in atmospheric, ground and ash cloud conditions (Fig. 9d and e). Fewer ash-containing pixels are correctly identified when the grainsize is coarser and the retrieved effective radius is an underestimate. An infrared image may show the presence of cooler material in the ash-filled pixels and visible imagery may show scatter from the aerosols, which a forecaster may be able to recognise in an operational VAAC setting, but it would not be detected by an automatic BTM method and therefore no retrievals would be automatically performed.

Figure 10 shows the relationship between the mass median radius of the input PSD and the retrieved effective radius. There is large scatter in the retrieved effective radii, due to variations in the atmospheric and volcanic plume conditions. The mean value follows the theoretical line until the mass median radius increases beyond $\sim 10\ \mu\text{m}$. At larger sizes, the mean retrieved effective radius is lower than the theoretical effective radius and the underestimation increases as the mass median radius increases. The mean retrieved effective radius reaches a plateau at around $9\ \mu\text{m}$ as the infrared retrievals have reducing sensitivity to the increasing proportion of larger particles. This may explain a lack of published retrieved effective radii greater than this value (Grainger et al., 2013). As the mass median radius of the PSD increases it is increasingly difficult to find a solution to the retrieval problem as the sensitivity to the larger particles decreases. Where an increasing proportion of larger particles are present, ash-containing pixels are only detected by additional tests using extra information (e.g. use of $8.7\ \mu\text{m}$ brightness temperatures; Francis et al., 2012); these would be missed by methods relying solely on the BTM. Fewer ash-containing pixels with low levels of uncertainty (low cost values) were present, so the density of values for these sizes is lower. At the largest grainsizes, many retrievals result in an effective radius close to the a priori value set in the retrieval problem of $3.5\ \mu\text{m}$.

The percentage of the input mass retrieved for a given mass median radius of the size distribution is shown in Fig. 11. The dashed line shows data from pixels correctly identified as containing ash and represents the accuracy of the retrieval method. The solid line compares the total ash input from the NAME model with the total mass re-

Big grains go far

J. A. Stevenson et al.

Title Page

Abstract

Introduction

Conclusions

References

Tables

Figures



Back

Close

Full Screen / Esc

Printer-friendly Version

Interactive Discussion



trieved and is sensitive to both the detection method and the retrieval method. Here, a cut-off mass loading value of 0.2 g m^{-2} was used. This is equivalent to a concentration of 0.2 mg m^{-3} for a 1 km ash cloud, which is the minimum concentration recorded on the ash concentration charts issued as supplementary charts by the London VAAC and the minimum that can be reliably detected by satellite remote sensing (Prata and Prata, 2012). For PSD with small geometric mass median radius of 1–2 μm , the detection and retrieval steps work very well and $\sim 100\%$ of mass is retrieved. As the geometric mass median radius increases the accurate identification of ash-contaminated pixels steadily decreases, with an approximately linear decrease of 5 % per unit increase in geometric mass median radius. The retrievals tend to overestimate the mass loading for PSD with geometric mass median radii 6–10 μm by up to 60 %. At greater particle sizes the retrieved mass loadings decrease, so the combined effect of underestimated detection and underestimated retrievals result in the mass loadings being increasingly underestimated. For a PSD with a mass median radius of 12 μm only $\sim 65\%$ of the mass is retrieved from pixels where ash is detected. This reduces to $< 25\%$ when considering all ash-contaminated pixels as many pixels that contain large ash particles are no longer identified.

5 Discussion

5.1 Distal transport of cryptotephra

Icelandic cryptotephra are found across NW Europe and provide information on the grainsize of particles carried to distal regions in volcanic plumes. The PSD for cryptotephra long axis lengths in the UK are lognormal, with very small proportions of particles small enough to contribute to the BTM effect. The sizes are consistent with single-grain measurements from around the world and with distal grainsize distributions from much larger eruptions (Table 1). Most damaging ash-aircraft encounters occur within 24 h of the onset of an eruption (Guffanti et al., 2010). At wind velocities observed dur-

Big grains go far

J. A. Stevenson et al.

Title Page

Abstract

Introduction

Conclusions

References

Tables

Figures



Back

Close

Full Screen / Esc

Printer-friendly Version

Interactive Discussion



ing recent eruptions (Table 4), an ash plume could travel 500–1600 km in this time and our model results confirm the potential for cryptotephra-sized grains to remain airborne to these distances, even from moderately-sized eruptions. The transport models also highlight the moderate effect of incorporating sphericity, density and atmospheric stratification on terminal velocity calculations. The effect of using measured fall velocities from Riley et al. (2003) is even larger and can result in a 3× increase in particle travel range compared to dense spheres (Note: uncertainty on this figure may be high as error data were not available). When comparing volcanic ash grains of different compositions, our calculations also show that rhyolite grains are more likely to reach the UK than basaltic ones (see Fig. 12), which may partly explain the dominance of rhyolitic grains in European cryptotephra, despite explosive basaltic eruptions being more common in Iceland (Lawson et al., 2012).

The proportion of cryptotephra-sized grains in a distal ash cloud is not well constrained; this is an important question in understanding distal transport of volcanic ash. Cryptotephra grain size distributions indicate that grains that are too coarse to contribute to the BTD effect must be present within the plume at distances over 500–1000 km from the source volcano, and in relatively larger quantities closer to the vent. Satellite retrievals suggest that the plume PSD is dominated by much smaller particles. The exact (small) proportion of cryptotephra-sized grains implied by a published r_{eff} can only be calculated if both the effective radius and the geometric standard deviation of the lognormal distributions are reported.

Satellite PSDs overlap with the lower size range of cryptotephra PSDs. For example, Prata and Prata (2012) retrieved an r_{eff} of 5.6 μm for an ash cloud near the Faroe Islands from Eyjafjallajökull eruption on 15 April 2010. Assuming a lognormal distribution with $\sigma = 2.0$, 50 % of the plume mass is contained in particles < 14.3 μm in diameter (and up to 95 % is within particles < 44.5 μm). This is compatible with the modal equivalent area diameter of particles deposited in the Faroe Islands by the Eyjafjallajökull eruption (see Fig. 2b), but does not account for the largest particles or aggregates (> 100 μm ; Stevenson et al., 2012).

5.2 Limitations of aircraft measurements of volcanic ash PSD

Published PSDs for airborne ash clouds are mostly limited to distal plumes, or to areas of low ash concentration around the plume margins. For example, the plume from the Eyjafjallajökull 2010 eruption was sampled by the UK's Facility for Airborne Atmospheric Measurements (FAAM) aircraft and by the Deutsches Zentrum für Luft- und Raumfahrt (DLR) Falcon aircraft. Both aircraft used wing-mounted sensors that estimate the grainsize of particles via optical scattering with nominal ranges of 0.6–50 μm (CAS instrument on FAAM) and 1–25 μm (FSSP-300 instrument on DLR Falcon). They also carried cloud imaging probes (CIP-15 with size range 15–930 μm on FAAM and 2D-C with range 25–800 μm on the DLR Falcon) that could detect much larger particles. Neither aircraft sampled the most concentrated parts of the plume during or immediately after the most explosive phases of the eruption (14–17 April, 5–6 May; Gudmundsson et al., 2012). FAAM reported that the most-concentrated ash ($> 600 \mu\text{g m}^{-3}$) was measured 700 km down wind on 14 May 2010 and contained particles up to 35 μm diameter (Johnson et al., 2012). The DLR Falcon sampled the plume repeatedly, recording concentrations up to $765 \mu\text{g m}^{-3}$ with grainsizes up to $\sim 20 \mu\text{m}$ diameter (Schumann et al., 2010). In both cases, much coarser particles were detected associated with meteorological clouds, but these were interpreted as water/ice. In another example, volcanic ash particles were identified on the air filters of the cabin cooling system of the NASA DC-8 aircraft that flew through ash from the Hekla 2000 eruption at a distance of 1500 km from the volcano. Ash grains were 1–10 μm in length (Pieri et al., 2002), but it is not clear if this is representative of the size in the cloud.

The lack of coarser cryptotephra-sized grains in these results may be a consequence of sampling during weak phases of eruptions and outside the highest concentration regions in the centre of the plume. The coarsest grains are likely to be deposited from the climactic phases of eruptions and from the most concentrated parts of their plumes. Alternatively, coarser ash grains may be associated with ice as hydrometeors (Durant

Big grains go far

J. A. Stevenson et al.

Title Page

Abstract

Introduction

Conclusions

References

Tables

Figures



Back

Close

Full Screen / Esc

Printer-friendly Version

Interactive Discussion



et al., 2009), especially during subglacial eruptions where large quantities of water are present at the vent.

The grainsize distribution within more concentrated plumes closer to the volcanoes was measured by Hobbs et al. (1991). A 10 km high plume from Mt Redoubt was sampled on 8 January 1990 at a location 130 km downwind, when the cloud was 2.5 h old. Measurements were made with a forward light scattering particle size instrument with a nominal stated range of 2–47 μm . The measured distribution contains particles of all sizes from $< 1 \mu\text{m}$ and is dominated by those in the 10–30 μm size range. However, there is evidence that this does not represent the true size distribution within the plume.

The shape of the size distribution (and those from the Mt St Helens and St Augustine eruptions, also measured by Hobbs et al., 1991) shows that it has been truncated so as to contain no particles coarser than 40 μm . This is due to the upper size limit of the instrument and is why all emission fluxes were reported as corresponding to particles $< 48 \mu\text{m}$ diameter. In fact, it can be expected that 50% of the material erupted during a short-lived, subplinian andesite eruption such as the 8 January 1990 Redoubt eruption, will have a grainsize coarser than 100 μm (e.g. Mt Spurr 1992; Durant et al., 2009), and that these particles will still be airborne after just 2.5 h (Fig. 12). This was demonstrated by the encounter between flight KLM867 and the ash from a previous eruption of Mt Redoubt on 15 December 1989, which took place further downwind, at a distance of 280 km from the volcano. Analysis of the aircraft found “heavy contamination” of the engine oil with particles up to 60 μm and a “substantial population” of 100 μm particles on the aircraft exterior (Casadevall, 1994). Thus the distributions presented in Hobbs et al. (1991) underestimate the concentration of cryptotephra-sized particles (and coarser) in the airborne plume. This is important because they are commonly used by VAACs to initialise atmospheric dispersion models (e.g. Webster et al., 2012).

Big grains go far

J. A. Stevenson et al.

Title Page

Abstract

Introduction

Conclusions

References

Tables

Figures



Back

Close

Full Screen / Esc

Printer-friendly Version

Interactive Discussion



5.3 Factors affecting satellite retrievals

Analysis of simulated satellite images presented here shows that retrieved effective radii are systematically underestimated in clouds with mass median radii greater than $\sim 10 \mu\text{m}$. This discrepancy arises because the retrieval problem is ill-posed, with many possible combinations of r_{eff} , mass loading, cloud height and meteorological parameters that would cause the observed (or simulated) BTM signal. The retrieval algorithm finds that a solution involving a lower mass loading of smaller particles (which contribute strongly to BTM effect) has a lower cost than a higher mass loading of a coarse PSD in which only a small proportion of grains contribute to the BTM effect. Our results apply to the method of Francis et al. (2012), but the significantly higher sensitivity of the BTM method to the finest grain sizes and the absence of published r_{eff} values greater than $10 \mu\text{m}$, even in proximal plumes, indicate that it is likely to be a feature of all similar retrieval algorithms. The results also highlight how incorporating meteorological information and brightness temperatures from other infrared channels allows ash-containing pixels to be identified that would otherwise be missed using the BTM method alone. As hyperspectral infrared satellite data become more widely available (e.g. Gangale et al., 2010), using information from the extra bands may better constrain retrievals.

Systematic underestimation of ash cloud mass is a result of both the reduced detection rate of ash-filled pixels containing large particles and the under-estimation of the mass loading within pixels that are correctly identified as ash-filled but that contain large particles. This has implications for our understanding of plume processes, as satellite data are used to track decreasing plume mass via deposition and to estimate the proportion transported to distal areas (Rose et al., 2000, 2001). This informs our understanding of ash cloud processes. Reliable data are also important for aviation safety. The London VAAC uses estimates of the distally transported mass proportion to initialise the NAME dispersion model (Webster et al., 2012). Satellite-derived mass loadings are also increasingly used directly for advice to the aviation industry and in

Title Page

Abstract

Introduction

Conclusions

References

Tables

Figures



Back

Close

Full Screen / Esc

Printer-friendly Version

Interactive Discussion



inversion modelling (e.g. Stohl et al., 2011). It is therefore important that the bias towards small particle sizes and low mass loadings is incorporated into any interpretation of satellite retrievals.

Meteorological factors complicate retrievals, both in simulations and real-life clouds. The main effect is to add noise, causing the retrieved r_{eff} from a single input distribution to have a range of values. For this reason, we recommend that histograms of retrieved effective radius from many pixels across the cloud should not be presented in a manner in which they could be mistaken for the grainsize distribution in the cloud. In a real plume, high atmospheric water vapour loading can produce positive BTDs, while temperature inversions above ice-covered land surfaces can produce negative BTDs (Prata et al., 2001). Furthermore, the presence of volcanic gases or ice forming upon ash particles may also affect the BTD signal.

The simulations consider an idealised situation where ash particles are dense spheres. Recently, investigations of the optical properties of non-spherical, vesicular particles using computer models shows that irregular particles can produce negative BTD at coarser grainsizes (up to 20 μm) than dense spheres (Kylling et al., 2014). The same study also concludes that the the assumption of dense spherical particles can underestimate the retrieved mass by 30 % compared with porous spheres and that uncertainty in particle shape increases the error to 50 %. This is a physical factor that may contribute to the limited range of published retrieved effective radii and may also explain why retrievals are possible from proximal clouds that should be too coarse to exhibit a BTD effect (e.g. Ruapehu 1996, Eyjafjallajökull 2010, Prata and Grant, 2001; Bonadonna et al., 2011). Thus, these errors should be taken into account when using retrievals that have used the dense sphere assumption. Real ash particles (such as those in Fig. 4) are even more irregular than those modelled by Kylling et al. (2014). It may be possible for a platy ash shard 5 μm thick to exhibit the BTD effect, despite having a length and width that would be reported by tephrochronologists of 50–100 μm . Current refractive index data have been measured from thin sections (e.g. Pollack et al., 1973) or from grains sieved to less than < 22.5 μm in size (Grainger et al., 2013). Fur-

Big grains go far

J. A. Stevenson et al.

Title Page

Abstract

Introduction

Conclusions

References

Tables

Figures

◀

▶

◀

▶

Back

Close

Full Screen / Esc

Printer-friendly Version

Interactive Discussion



ther quantitative, empirical data on the optical properties of ash samples of varied size, shape and composition are required to better-constrain this effect. Given the large difference between fall velocities of real and simulated ash particles, these would ideally be combined with measurements of aerodynamic properties, thus improving dispersion modelling inputs, too.

6 Conclusions

We suggest four reasons for the discrepancy between the size of volcanic ash particles reported by tephrochronologists and by satellite remote sensing. The first is the way that tephrochronologists measure and report grainsize. The long axis length measurements made by tephrochronologists are around $1.5\times$ the equivalent area diameter of the same particles. Furthermore, as cryptotephra size distributions are lognormal, reporting the arithmetic mean grainsize as opposed to the geometric mean gives the impression that the modal grainsize is larger than it is. However, comparison of grain-size distributions measured manually by optical microscope and by laser particle size analyser demonstrates that modal grainsize is still captured correctly by manual measurements and so difficulty in identifying the smallest grains is not a large source of error in reported cryptotephra sizes.

The second reason is that r_{eff} represents a size distribution extending to much coarser grain sizes. For example, where $r_{\text{eff}} = 8\ \mu\text{m}$ and the geometric standard deviation, σ is 2.0, 95% of the mass is contained in particles $< 64\ \mu\text{m}$. For this reason, σ should always be reported alongside r_{eff} values and histograms of r_{eff} should not be presented in a way that could be misunderstood as a PSD. Cryptotephra grains may therefore be represented by the coarse tail of the distribution and distal aircraft measurements of dilute ash clouds from weak eruptions are consistent with this. It should be noted that there are no reliable published grainsize distributions obtained by direct sampling within concentrated (e.g. $1\ \text{g m}^{-3}$) ash clouds. Cryptotephra grains within the coarse tail of the distribution cannot be the whole explanation, however, as r_{eff} values

Big grains go far

J. A. Stevenson et al.

Title Page

Abstract

Introduction

Conclusions

References

Tables

Figures



Back

Close

Full Screen / Esc

Printer-friendly Version

Interactive Discussion



of 10–17, which are theoretically possible, are not reported in the literature, even for proximal clouds.

Here we highlight a third reason: low r_{eff} values can result from the systematic underestimation by retrieval algorithms. This occurs because solutions with low masses dominated by small particles, to which the infrared data are more sensitive, are preferable to those with high masses dominated by large particles. The combined effect of undetected pixels and underestimation of retrieved mass loading causes over 50 % of the mass of the cloud to be missed. This is an important consideration for VAACs, yet it is still insufficient to explain the 10× discrepancy between ground- and satellite-based estimates of deposit mass in proximal areas.

The fourth reason is the physics of infrared scattering by vesicular and highly irregular volcanic ash particles. As recently highlighted by Kylling et al. (2014), using the dense spheres approximation underestimates the size of particles that are able to contribute to the BTD effect. The largest distal tephra grains have a platy morphology and can be 50–100 μm long, but < 5 μm thick; it may be possible that they contribute to the BTD effect in certain orientations. Under the dense spheres approximation, these would be interpreted as having a diameter of < 12 μm. We suggest that empirical, quantitative studies into the optical and aerodynamic properties of volcanic ash grains of varied composition and size are essential to address this problem.

Appendix A: Particle size distributions and the effective radius

The size distribution of airborne volcanic ash is typically modelled as lognormal, as defined by Eq. (A1).

$$n(r) = \frac{N_0}{\sqrt{2\pi}} \frac{1}{\ln(\sigma)} \frac{1}{r} \exp\left(-\frac{(\ln r - \ln r_m)^2}{2\ln^2(\sigma)}\right) \quad (\text{A1})$$

where N_0 is the total number density, r is the particle radius and r_m is the number median radius (which is equal to the number *geometric* mean radius). There is frequently

Title Page

Abstract

Introduction

Conclusions

References

Tables

Figures

◀

▶

◀

▶

Back

Close

Full Screen / Esc

Printer-friendly Version

Interactive Discussion



Big grains go far

J. A. Stevenson et al.

Title Page

Abstract

Introduction

Conclusions

References

Tables

Figures

◀

▶

◀

▶

Back

Close

Full Screen / Esc

Printer-friendly Version

Interactive Discussion



confusion, particularly across different subjects, in the meaning of σ and so care must be taken when comparing size distributions in the literature. In this formulation, σ is the *geometric* standard deviation, such that $\ln(\sigma)$ is the standard deviation of the logarithms of the grain sizes, and 95.5% of the distribution lies within the range r_n/σ^2 to $r_n \times \sigma^2$ (Limpert et al., 2001). Values of σ of ~ 2 are commonly used to describe the PSD of volcanic ash clouds (Pavolonis et al., 2013).

It can be shown that the particle size distribution in terms of mass is also lognormal (Seinfeld and Pandis, 2006), with the same geometric standard deviation, σ , and with a mass median radius r_m related to the number median radius r_n by:

$$r_m = r_n \exp(3\ln^2 \sigma) \quad (\text{A2})$$

The effective radius is the size of particle in a uniformly-sized suspension of that scatters infrared in an equivalent manner to the combined effect of all particle sizes in a size distribution. It is calculated by Eq. (A3).

$$r_{\text{eff}} = \frac{\int_0^{\infty} r^3 n(r) dr}{\int_0^{\infty} r^2 n(r) dr} \quad (\text{A3})$$

where r is the particle radius and $n(r)$ is the number density per unit radius. The effective radius for the lognormal size distribution in terms of number median radius and geometric standard deviation is:

$$r_{\text{eff}} = r_n \exp\left(\frac{5}{2}\ln^2 \sigma\right) \quad (\text{A4})$$

For a PSD with geometric standard deviation (σ) of 2.0, the effective radius is therefore equal to $3.32 \times$ the number median radius (r_n) and $0.79 \times$ the mass median radius (r_m). Curves showing the grain size distributions that correspond to different effective radii are shown in Fig. 1.

Appendix B: Equations for terminal velocity of non-spherical particles

The terminal fall velocity (W_T) of a single particle falling in air is given by Eq. (B1) (Maryon et al., 1999).

$$W_T = \left(\frac{4}{3} \frac{D}{C_D} g \frac{\rho_P - \rho}{\rho} \right)^{1/2} \quad (\text{B1})$$

D is the particle diameter, C_D is the drag coefficient, g is gravitational acceleration, ρ is fluid density and ρ_P is particle density. Equation (B1) can be applied to all particle shapes and Reynolds numbers (Re) by defining an appropriate drag coefficient (C_D) and taking the particle diameter to be that of an equivalent sphere with the same volume (D_v). For spherical particles at low Reynolds numbers (i.e. $Re \ll 1$), $C_D = 24/Re$ and Eq. (B1) simplifies to Stokes' law. This was used for the simplest scheme and is appropriate for particles up to 100 μm diameter. For the more realistic scenario, the drag coefficient (C_D) for non-spherical particles was calculated using the scheme presented by Ganser (1993) as recommended by Alfano et al. (2011) and described by Eq. (B2).

$$C_D = \frac{24}{ReK_1} \left(1 + 0.1118[Re(K_1K_2)]^{0.6567} \right) + \frac{0.4305K_2}{1 + \frac{3305}{ReK_1K_2}} \quad (\text{B2})$$

$$K_1 = \frac{3}{1 + 2\Psi_R^{-0.5}} \quad (\text{B3})$$

$$K_2 = 10^{1.84148(-\log \Psi_R)^{0.5743}} \quad (\text{B4})$$

$Re = \frac{\rho W_T D_v}{\eta}$ is the Reynolds number and η is the fluid viscosity. The particle morphology is characterised using the sphericity parameter (Ψ_R), which is defined in 2-dimensions by Riley et al. (2003, Eq. B5) as the ratio between the projected area (A_P) and the



square of the projected perimeter (P_P):

$$\Psi_R = \frac{4\pi A_P}{P_P^2} \quad (\text{B5})$$

**The Supplement related to this article is available online at
doi:10.5194/amtd-8-65-2015-supplement.**

5 *Acknowledgements.* J. A. Stevenson is funded by The Royal Society of Edinburgh via a Scot-
tish Government/Marie Curie Actions Personal Research Fellowship. The Askja 1875 sample
was provided by Jan Mangerud. Andrew Bell had useful comments on fitting particle size distri-
butions. The RTTOV model is developed as part of the EUMETSAT-funded NWP SAF activities.
F. M. Beckett would like to thank Claire Witham, Matthew Hort and the ADAQ group at the Met
10 Office for their support and guidance. S. C. Millington would like to thank Pete Francis for his
guidance throughout this work. We thank three anonymous reviewers for their comments on
a previous version of the manuscript.

References

- 15 Abbott, P. and Davies, S.: Volcanism and the Greenland ice-cores: the tephra record, *Earth-Sci.*
Rev., 115, 173–191, doi:10.1016/j.earscirev.2012.09.001, 2012. 68, 75
- Abbott, P. M., Davies, S. M., Steffensen, J. P., Pearce, N. J. G., Bigler, M., Johnsen, S. J.,
Seierstad, I. K., Svensson, A., and Wastegard, S.: A detailed framework of marine isotope
stages 4 and 5 volcanic events recorded in two Greenland ice-cores, *Quaternary Sci. Rev.*,
36, 59–77, doi:10.1016/j.quascirev.2011.05.001, 2012. 104
- 20 Alfano, F., Bonadonna, C., Delmelle, P., and Costantini, L.: Insights on tephra set-
tling velocity from morphological observations, *J. Volcanol. Geoth. Res.*, 208, 86–98,
doi:10.1016/j.jvolgeores.2011.09.013, 2011. 93
- Bergman, J., Wastegard, S., Hammarlund, D., Wohlfarth, B., and Roberts, S.: Holocene tephra
horizons at Klocka Bog, west-central Sweden: aspects of reproducibility in subarctic peat
25 deposits, *J. Quaternary Sci.*, 19, 241–249, doi:10.1002/jqs.833, 2004. 104



Big grains go far

J. A. Stevenson et al.

Title Page

Abstract

Introduction

Conclusions

References

Tables

Figures



Back

Close

Full Screen / Esc

Printer-friendly Version

Interactive Discussion



- Blockley, S., Lane, C., Lotter, A., and Pollard, A.: Evidence for the presence of the Vedde Ash in Central Europe, *Quaternary Sci. Rev.*, 26, 3030–3036, doi:10.1016/j.quascirev.2007.09.010, 2007. 104
- Bonadonna, C. and Houghton, B.: Total grain-size distribution and volume of tephra-fall deposits, *B. Volcanol.*, 67, 441–456, 2005. 68, 71
- Bonadonna, C. and Phillips, J. C.: Sedimentation from strong volcanic plumes, *J. Geophys. Res.*, 108, 2340, doi:10.1029/2002JB002034, 2003. 78
- Bonadonna, C., Genco, R., Gouhier, M., Pistolesi, M., Cioni, R., Alfano, F., Hoskuldsson, A., and Ripepe, M.: Tephra sedimentation during the 2010 Eyjafjallajökull eruption (Iceland) from deposit, radar, and satellite observations, *J. Geophys. Res.-Sol. Ea.*, 116, B12202, doi:10.1029/2011JB008462, 2011. 72, 89
- Bramham-Law, C. W. F., Theuerkauf, M., Lane, C. S., and Mangerud, J.: New findings regarding the Saksunarvatn Ash in Germany, *J. Quaternary Sci.*, 28, 248–257, doi:10.1002/jqs.2615, 2013. 104, 110
- Carey, S. N. and Sigurdsson, H.: Influence of particle aggregation on deposition of distal tephra from the M₁₈, 1980, eruption of Mount St. Helens volcano, *J. Geophys. Res.-Sol. Ea.*, 87, 7061–7072, doi:10.1029/JB087iB08p07061, 1982. 110
- Casadevall, T. J.: The 1989–1990 eruption of Redoubt Volcano, Alaska: impacts on aircraft operations, *J. Volcanol. Geoth. Res.*, 62, 301–316, doi:10.1016/0377-0273(94)90038-8, 1994. 87
- Colette, A., Favez, O., Meleux, F., Chiappini, L., Haeffelin, M., Morille, Y., Malherbe, L., Papin, A., Bessagnet, B., Menut, L., Leoz, E., and Rouil, L.: Assessing in near real time the impact of the April 2010 Eyjafjallajökull ash plume on air quality, *Atmos. Environ.*, 45, 1217–1221, doi:10.1016/j.atmosenv.2010.09.064, 2011. 107
- Coulter, S. E., Turney, C. S. M., Kershaw, P., and Rule, S.: The characterization and significance of a MIS 5a distal tephra on mainland Australia, *Quaternary Sci. Rev.*, 28, 1825–1830, doi:10.1016/j.quascirev.2009.04.018, 2009. 104
- Coulter, S. E., Pilcher, J., Plunkett, G., Baillie, M., Hall, V., Steffensen, J., Vinther, B., Clausen, H., and Johnsen, S.: Holocene tephtras highlight complexity of volcanic signals in Greenland ice cores, *J. Geophys. Res.-Atmos.*, 117, D21303, doi:10.1029/2012JD017698, 2012. 104

Big grains go far

J. A. Stevenson et al.

Title Page

Abstract

Introduction

Conclusions

References

Tables

Figures

◀

▶

◀

▶

Back

Close

Full Screen / Esc

Printer-friendly Version

Interactive Discussion



- Dacre, H. F., Grant, A. L. M., and Johnson, B. T.: Aircraft observations and model simulations of concentration and particle size distribution in the Eyjafjallajökull volcanic ash cloud, *Atmos. Chem. Phys.*, 13, 1277–1291, doi:10.5194/acp-13-1277-2013, 2013. 69
- Davies, S., Turney, C., and Lowe, J.: Identification and significance of a visible, basalt-rich Vedde Ash layer in a Late-glacial sequence on the Isle of Skye, Inner Hebrides, Scotland, *J. Quaternary Sci.*, 16, 99–104, doi:10.1002/jqs.611, 2001. 104
- Davies, T., Cullen, M., Malcolm, A., Mawson, M., Staniforth, A., White, A. A., and Wood, N.: A new dynamical core for the Met Office's global and regional modelling of the atmosphere, *Q. J. Roy. Meteor. Soc.*, 608, 1759–1782, 2005. 81
- De Angelis, M., Fehrenbach, L., Jehanno, C., and Maurette, M.: Micrometre-sized volcanic glasses in polar ices and snows, *Nature*, 317, 52–54, doi:10.1038/317052a0, 1985. 75, 104
- Devenish, B., Thomson, D., Marengo, F., Leadbetter, S., Ricketts, H., and Dacre, H.: A study of the arrival over the United Kingdom in April 2010 of the Eyjafjallajökull ash cloud using ground-based lidar and numerical simulations, *Atmos. Environ.*, 48, 152–164, doi:10.1016/j.atmosenv.2011.06.033, 2012. 69
- Dugmore, A.: Icelandic volcanic ash in Scotland, *Scot. Geogr. Mag.*, 105, 168–172, doi:10.1080/14702548908554430, 1989. 68
- Dugmore, A., Newton, A., Edwards, K., Larsen, G., Blackford, J., and Cook, G.: Long-distance marker horizons from smallscale eruptions: British tephra deposits from the AD 1510 eruption of Hekla, Iceland, *J. Quaternary Sci.*, 11, 511–516, 1996. 74, 104
- Dunbar, N. W. and Kurbatov, A. V.: Tephrochronology of the Siple Dome ice core, West Antarctica: correlations and sources, *Quaternary Sci. Rev.*, 30, 1602–1614, doi:10.1016/j.quascirev.2011.03.015, 2011. 104
- Durant, A. J., Rose, W. I., Sarna-Wojcicki, A. M., Carey, S., and Volentik, A. C. M.: Hydrometeor-enhanced tephra sedimentation: constraints from the 18 May 1980 eruption of Mount St. Helens, *J. Geophys. Res.-Sol. Ea.*, 114, B03204, doi:10.1029/2008JB005756, 2009. 69, 86, 87, 104
- Durant, A. J., Villarosa, G., Rose, W. I., Delmelle, P., Prata, A. J., and Viramonte, J. G.: Long-range volcanic ash transport and fallout during the 2008 eruption of Chaiten volcano, Chile, *Phys. Chem. Earth*, 45–46, 50–64, doi:10.1016/j.pce.2011.09.004, 2012. 104
- Eliasson, J., Yoshitani, J., Weber, K., Yasuda, N., Iguchi, M., and Vogel, A.: Airborne measurement in the ash plume from Mount Sakurajima: analysis of gravitational effects

Big grains go far

J. A. Stevenson et al.

Title Page

Abstract

Introduction

Conclusions

References

Tables

Figures



Back

Close

Full Screen / Esc

Printer-friendly Version

Interactive Discussion



on dispersion and fallout, *International Journal of Atmospheric Sciences*, 2014, 1–16, doi:10.1155/2014/372135, 2014. 69

Engwell, S. L., Sparks, R. S. J., and Aspinall, W. P.: Quantifying uncertainties in the measurement of tephra fall thickness, *Journal of Applied Volcanology*, 2, 5, doi:10.1186/2191-5040-2-5, 2013. 74, 76, 104

Francis, P. N., Cooke, M. C., and Saunders, R. W.: Retrieval of physical properties of volcanic ash using Meteosat: a case study from the 2010 Eyjafjallajökull eruption, *J. Geophys. Res.-Atmos.*, 117, D00U09, doi:10.1029/2011JD016788, 2012. 70, 71, 80, 81, 82, 83, 88

Gangale, G., Prata, A., and Clarisse, L.: The infrared spectral signature of volcanic ash determined from high-spectral resolution satellite measurements, *Remote Sens. Environ.*, 114, 414–425, doi:10.1016/j.rse.2009.09.007, 2010. 70, 88

Ganser, G. H.: A rational approach to drag prediction of spherical and nonspherical particles, *Powder Technol.*, 77, 143–152, 1993. 78, 93

Grainger, R. G., Peters, D. M., Thomas, G. E., Smith, A. J. A., Siddans, R., Carboni, E., and Dudhia, A.: Measuring volcanic plume and ash properties from space, *Geol. Soc. Spec. Publ.*, 380, 293–320, doi:10.1144/SP380.7, 2013. 71, 83, 89

Gudmundsson, M. T., Thordarson, T., Höskuldsson, A., Larsen, G., Björnsson, H., Prata, F. J., Oddsson, B., Magnússon, E., Högnadóttir, T., Petersen, G. N., Hayward, C. L., Stevenson, J. A., and Jónsdóttir, I.: Ash generation and distribution from the April-May 2010 eruption of Eyjafjallajökull, Iceland, *Scientific Reports*, 2, 572, doi:10.1038/srep00572, 2012. 69, 72, 78, 86

Guffanti, M., Casadevall, T. J., and Budding, K.: Encounters of Aircraft with Volcanic Ash Clouds: A Compilation of Known Incidents, 1953–2009., Tech. rep., U.S. Geological Survey, 2010. 84

Hall, V. and Pilcher, J.: Late-quaternary Icelandic tephra in Ireland and Great Britain: detection, characterization and usefulness, *Holocene*, 12, 223–230, 2002. 68, 73

Hayward, C.: High spatial resolution electron probe microanalysis of tephra and melt inclusions without beam-induced chemical modification, *Holocene*, 22, 119–125, doi:10.1177/0959683611409777, 2012. 68

Hobbs, P. V., Radke, L. F., Lyons, J. H., Ferek, R. J., Coffman, D. J., and Casadevall, T. J.: Airborne measurements of particle and gas emissions from the 1990 volcanic eruptions of Mount Redoubt, *J. Geophys. Res.-Atmos.*, 96, 18735–18752, doi:10.1029/91JD01635, 1991. 87

Big grains go far

J. A. Stevenson et al.

Title Page

Abstract

Introduction

Conclusions

References

Tables

Figures



Back

Close

Full Screen / Esc

Printer-friendly Version

Interactive Discussion



- Housley, R. A., MacLeod, A., Nalepka, D., Jurochnik, A., Masojć, M., Davies, L., Lincoln, P. C., Bronk Ramsey, C., Gamble, C. S., and Lowe, J. J.: Tephrostratigraphy of a Lateglacial lake sediment sequence at Węgliny, southwest Poland, *Quaternary Sci. Rev.*, 77, 4–18, doi:10.1016/j.quascirev.2013.07.014, 2013. 77, 104, 110
- 5 Jensen, B. J. L., Pyne-O'Donnell, S., Plunkett, G., Froese, D. G., Hughes, P. D. M., Sigl, M., McConnell, J. R., Amesbury, M. J., Blackwell, P. G., van den Bogaard, C., Buck, C. E., Charman, D. J., Clague, J. J., Hall, V. A., Koch, J., Mackay, H., Mallon, G., McColl, L., and Pilcher, J. R.: Transatlantic distribution of the Alaskan White River Ash, *Geology*, 42, 875–878, doi:10.1130/G35945.1, 2014. 74
- 10 Johnson, B., Turnbull, K., Brown, P., Burgess, R., Dorsey, J., Baran, A. J., Webster, H., Haywood, J., Cotton, R., Ulanowski, Z., Hesse, E., Woolley, A., and Rosenberg, P.: In situ observations of volcanic ash clouds from the FAAM aircraft during the eruption of Eyjafjallajökull in 2010, *J. Geophys. Res.-Atmos.*, 117, D00U24, doi:10.1029/2011JD016760, 2012. 76, 81, 86
- 15 Jones, A., Thomson, D., Hort, M., and Devenish, B.: The U.K. Met Office's Next-Generation Atmospheric Dispersion Model, NAME III, in: *Air Pollution Modeling and Its Application XVII*, edited by: Borrego, C. and Norman, A.-L., 580–589, Springer US, Boston, MA, 2006. 81
- Kylling, A., Buras, R., Eckhardt, S., Emde, C., Mayer, B., and Stohl, A.: Simulation of SEVIRI infrared channels: a case study from the Eyjafjallajökull April/May 2010 eruption, *Atmos. Meas. Tech.*, 6, 649–660, doi:10.5194/amt-6-649-2013, 2013. 80
- 20 Kylling, A., Kahnert, M., Lindqvist, H., and Nousiainen, T.: Volcanic ash infrared signature: porous non-spherical ash particle shapes compared to homogeneous spherical ash particles, *Atmos. Meas. Tech.*, 7, 919–929, doi:10.5194/amt-7-919-2014, 2014. 70, 89, 91
- Lane, C. S., Andric, M., Cullen, V. L., and Blockley, S. P. E.: The occurrence of distal Icelandic and Italian tephra in the Lateglacial of Lake Bled, Slovenia, *Quaternary Sci. Rev.*, 30, 1013–1018, doi:10.1016/j.quascirev.2011.02.014, 2011. 77, 104
- 25 Lane, C. S., Blockley, S. P. E., Mangerud, J., Smith, V. C., Lohne, O. S., Tomlinson, E. L., Matthews, I. P., and Lotter, A. F.: Was the 12.1 ka Icelandic Vedde Ash one of a kind?, *Quaternary Sci. Rev.*, 33, 87–99, doi:10.1016/j.quascirev.2011.11.011, 2012. 74, 110
- 30 Lavigne, F., Degeai, J.-P., Komorowski, J.-C., Guillet, S., Robert, V., Lahitte, P., Oppenheimer, C., Stoffel, M., Vidal, C. M., Surono, Pratomo, I., Wassmer, P., Hajdas, I., Hadmoko, D. S., and de Belizal, E.: Source of the great A.D. 1257 mystery eruption unveiled, Samalas vol-

Big grains go far

J. A. Stevenson et al.

Title Page

Abstract

Introduction

Conclusions

References

Tables

Figures

◀

▶

◀

▶

Back

Close

Full Screen / Esc

Printer-friendly Version

Interactive Discussion



cano, Rinjani Volcanic Complex, Indonesia, P. Natl. Acad. Sci. USA, 110, 16742–16747, doi:10.1073/pnas.1307520110, 2013. 75, 104

Lawson, I. T., Swindles, G. T., Plunkett, G., and Greenberg, D.: The spatial distribution of Holocene cryptotephra in north-west Europe since 7ka: implications for understanding ash fall events from Icelandic eruptions, *Quaternary Sci. Rev.*, 41, 57–66, doi:10.1016/j.quascirev.2012.02.018, 2012. 85, 110

Leadbetter, S. J. and Hort, M. C.: Volcanic ash hazard climatology for an eruption of Hekla Volcano, Iceland, *J. Volcanol. Geoth. Res.*, 199, 230–241, doi:10.1016/j.jvolgeores.2010.11.016, 2011. 79

Limpert, E., Stahel, W. A., and Abbt, M.: Log-normal distributions across the sciences: keys and clues, *Bioscience*, 51, 341–352, 2001. 92

Lowe, D. J.: Tephrochronology and its application: a review, *Quat. Geochronol.*, 6, 107–153, doi:10.1016/j.quageo.2010.08.003, 2011. 68

Maryon, R., Ryall, D., and Malcolm, A.: The NAME 4 dispersion model: Science documentation, Met Office turbulence and diffusion note, 262, 45, 1999. 93

Matricardi, M.: The inclusion of aerosols and clouds in RTIASI, the ECMWF fast radiative transfer model for the Infrared Atmospheric Sounding Interferometer, “Technical Memorandum” 474, ECMWF, available at: <http://old.ecmwf.int/publications/library/do/references/list/14> (last access: 19 December 2014), 2005. 80

Matthews, N. E., Smith, V. C., Costa, A., Durant, A. J., Pyle, D. M., and Pearce, N. J. G.: Ultra-distal tephra deposits from super-eruptions: examples from Toba, Indonesia and Taupo Volcanic Zone, New Zealand, *Quaternary Int.*, 258, 54–79, doi:10.1016/j.quaint.2011.07.010, 2012. 74, 104

Millington, S. C., Saunders, R., Francis, P., and Webster, H. N.: Simulated volcanic ash imagery: a method to compare NAME ash concentration forecasts with SEVIRI imagery for the Eyjafjallajökull eruption in 2010, *J. Geophys. Res.-Atmos.*, 117, D00U1, doi:10.1029/2011JD016770, 2012. 80

Mortensen, A., Bigler, M., Grönvold, K., Steffensen, J., and Johnsen, S.: Volcanic ash layers from the last glacial termination in the NGRIP ice core, *J. Quaternary Sci.*, 20, 209–219, doi:10.1002/jqs.908, 2005. 75, 104

Newhall, C. G. and Self, S.: The Volcanic Explosivity Index (VEI) an estimate of explosive magnitude for historical volcanism, *J. Geophys. Res.*, 87, 1231–1238, doi:10.1029/JC087iC02p01231, 1982. 74, 104

Big grains go far

J. A. Stevenson et al.

Title Page

Abstract

Introduction

Conclusions

References

Tables

Figures



Back

Close

Full Screen / Esc

Printer-friendly Version

Interactive Discussion



- Newton, A. J., Dugmore, A. J., and Gittings, B. M.: Tephrobase: tephrochronology and the development of a centralised European database, *J. Quaternary Sci.*, 22, 737–743, doi:10.1002/jqs.1094, 2007. 74
- Palais, J. M., Germani, M. S., and Zielinski, G. A.: Inter-hemispheric transport of volcanic ash from a 1259 A.D. volcanic eruption to the Greenland and Antarctic Ice Sheets, *Geophys. Res. Lett.*, 19, 801–804, doi:10.1029/92GL00240, 1992. 75, 104
- Pavolonis, M. J., Feltz, W. F., Heidinger, A. K., and Gallina, G. M.: A daytime complement to the reverse absorption technique for improved automated detection of volcanic ash, *J. Atmos. Ocean. Tech.*, 23, 1422–1444, doi:10.1175/JTECH1926.1, 2006. 80
- Pavolonis, M. J., Heidinger, A. K., and Sieglaff, J.: Automated retrievals of volcanic ash and dust cloud properties from upwelling infrared measurements, *J. Geophys. Res.-Atmos.*, 118, 1436–1458, doi:10.1002/jgrd.50173, 2013. 70, 71, 81, 92
- Persson, C.: Tephrochronological investigation of peat deposits in Scandinavia and on the Faroe Islands, Sveriges reproduktions AB (distr.), 1971. 68, 74, 105, 111
- Petersen, G. N., Bjornsson, H., and Arason, P.: The impact of the atmosphere on the Eyjafjalajökull 2010 eruption plume, *J. Geophys. Res.*, 117, D00U07, doi:10.1029/2011JD016762, 2012. 78
- Pieri, D., Ma, C., Simpson, J. J., Hufford, G., Grindle, T., and Grove, C.: Analyses of in-situ airborne volcanic ash from the February 2000 eruption of Hekla Volcano, Iceland, *Geophys. Res. Lett.*, 29, 19.1–19.4, doi:10.1029/2001GL013688, 2002. 86
- Pollack, J. B., Toon, O. B., and Khare, B. N.: Optical properties of some terrestrial rocks and glasses, *Icarus*, 19, 372–389, doi:10.1016/0019-1035(73)90115-2, 1973. 70, 80, 82, 89
- Prata, A. J.: Infrared radiative transfer calculations for volcanic ash clouds, *Geophys. Res. Lett.*, 16, 1293–1296, doi:10.1029/GL016i011p01293, 1989. 69, 71
- Prata, A. J. and Grant, I. F.: Retrieval of microphysical and morphological properties of volcanic ash plumes from satellite data: application to Mt Ruapehu, New Zealand, *Q. J. Roy. Meteor. Soc.*, 127, 2153–2179, doi:10.1002/qj.49712757615, 2001. 72, 89
- Prata, A. J. and Prata, A. T.: Eyjafjallajökull volcanic ash concentrations determined using Spin Enhanced Visible and Infrared Imager measurements, *J. Geophys. Res.*, 117, D00U23, doi:10.1029/2011JD016800, 2012. 70, 71, 84, 85
- Prata, F., Bluth, G., Rose, B., Schneider, D., and Tupper, A.: Comments on “Failures in detecting volcanic ash from a satellite-based technique”, *Remote Sens. Environ.*, 78, 341–346, doi:10.1016/S0034-4257(01)00231-0, 2001. 89

Big grains go far

J. A. Stevenson et al.

Title Page

Abstract

Introduction

Conclusions

References

Tables

Figures



Back

Close

Full Screen / Esc

Printer-friendly Version

Interactive Discussion



- Pyne-O'Donnell, S. D., Hughes, P. D., Froese, D. G., Jensen, B. J., Kuehn, S. C., Mallon, G., Amesbury, M. J., Charman, D. J., Daley, T. J., Loader, N. J., Mauquoy, D., Street-Perrott, F. A., and Woodman-Ralph, J.: High-precision ultra-distal Holocene tephrochronology in North America, *Quaternary Sci. Rev.*, 52, 6–11, doi:10.1016/j.quascirev.2012.07.024, 2012. 104
- 5 Riley, C., Rose, W., and Bluth, G.: Quantitative shape measurements of distal volcanic ash, *J. Geophys. Res.-Sol. Ea.*, 108, 2504, doi:10.1029/2001JB000818, 2003. 69, 76, 78, 79, 85, 93, 104, 114, 120
- Rose, W. and Durant, A.: Fine ash content of explosive eruptions, *J. Volcanol. Geoth. Res.*, 186, 32–39, 2009. 68
- 10 Rose, W. I., Bluth, G. J. S., and Ernst, G. G. J.: Integrating retrievals of volcanic cloud characteristics from satellite remote sensors: a summary, *Philos. T. Roy. Soc. A*, 358, 1585–1606, doi:10.1098/rsta.2000.0605, 2000. 69, 88
- Rose, W. I., Bluth, G. J. S., Schneider, D. J., Ernst, G. G. J., Riley, C. M., Henderson, L. J., and McGimsey, R. G.: Observations of volcanic clouds in their first few days of atmospheric residence: the 1992 eruptions of Crater Peak, Mount Spurr Volcano, Alaska, *J. Geol.*, 109, 677–694, doi:10.1086/323189, 2001. 69, 70, 81, 88
- 15 Rose, W. I., Riley, C., and Darteville, S.: Sizes and shapes of 10-Ma distal fall pyroclasts in the Ogallala Group, Nebraska, *J. Geol.*, 111, 115–124, doi:10.1086/344668, 2003. 69
- Rust, A. C. and Cashman, K. V.: Permeability controls on expansion and size distributions of pyroclasts, *J. Geophys. Res.*, 116, B11202, doi:10.1029/2011JB008494, 2011. 68, 69
- 20 Saunders, R., Hocking, J., Rayer, P., Matricardi, M., Geer, A., Bormann, N., Brunel, P., Karbou, F., and Aires, F.: RTTOV-10 Science and Validation Report, available at: <http://research.metoffice.gov.uk/research/interproj/nwpsaf/rtm/> (last access: 19 December 2014), 2012. 80
- Scasso, R. A., Corbella, H., and Tiberi, P.: Sedimentological analysis of the tephra from the 12–15 August 1991 eruption of Hudson volcano, *B. Volcanol.*, 56, 121–132, doi:10.1007/BF00304107, 1994. 104
- 25 Schumann, U., Weinzierl, B., Reitebuch, O., Schlager, H., Minikin, A., Forster, C., Baumann, R., Sailer, T., Graf, K., Mannstein, H., Voigt, C., Rahm, S., Simmet, R., Scheibe, M., Lichtenstern, M., Stock, P., Rüba, H., Schäuble, D., Tafferner, A., Rautenhaus, M., Gerz, T., Ziereis, H., Krautstrunk, M., Mallaun, C., Gayet, J.-F., Lieke, K., Kandler, K., Ebert, M., Weinbruch, S., Stohl, A., Gasteiger, J., Groß, S., Freudenthaler, V., Wiegner, M., Ansmann, A., Tesche, M., Olafsson, H., and Sturm, K.: Airborne observations of the Eyjafjalla volcano ash
- 30

Big grains go far

J. A. Stevenson et al.

Title Page

Abstract

Introduction

Conclusions

References

Tables

Figures



Back

Close

Full Screen / Esc

Printer-friendly Version

Interactive Discussion



cloud over Europe during air space closure in April and May 2010, *Atmos. Chem. Phys.*, 11, 2245–2279, doi:10.5194/acp-11-2245-2011, 2011. 86

Seinfeld, J. H. and Pandis, S. N.: *Atmospheric Chemistry and Physics: from Air Pollution to Climate Change*, Wiley-Interscience, Hoboken, NJ, 2nd edn., 2006. 67, 92

5 Stevenson, J. A., Loughlin, S., Rae, C., Thordarson, T., Milodowski, A. E., Gilbert, J. S., Harangi, S., Lukács, R., Højgaard, B., Ártíng, U., Pyne-O'Donnell, S., MacLeod, A., Whitney, B., and Cassidy, M.: Distal deposition of tephra from the Eyjafjallajökull 2010 summit eruption, *J. Geophys. Res.*, 117, B00C10, doi:10.1029/2011JB008904, 2012. 73, 74, 85, 104, 107

10 Stevenson, J. A., Loughlin, S. C., Font, A., Fuller, G. W., MacLeod, A., Oliver, I. W., Jackson, B., Horwell, C. J., Thordarson, T., and Dawson, I.: UK monitoring and deposition of tephra from the May 2011 eruption of Grímsvötn, Iceland, *Journal of Applied Volcanology*, 2, 3, doi:10.1186/2191-5040-2-3, 2013. 73, 74, 77, 104, 107

15 Stohl, A., Prata, A. J., Eckhardt, S., Clarisse, L., Durant, A., Henne, S., Kristiansen, N. I., Minikin, A., Schumann, U., Seibert, P., Stebel, K., Thomas, H. E., Thorsteinsson, T., Tørseth, K., and Weinzierl, B.: Determination of time- and height-resolved volcanic ash emissions and their use for quantitative ash dispersion modeling: the 2010 Eyjafjallajökull eruption, *Atmos. Chem. Phys.*, 11, 4333–4351, doi:10.5194/acp-11-4333-2011, 2011. 72, 89

Swindles, G. T., De Vleeschouwer, F., and Plunkett, G.: Dating peat profiles using tephra: stratigraphy, geochemistry and chronology, *Mires and Peats*, 7, 1–9, 2010. 68, 73

20 Swindles, G. T., Lawson, I. T., Savov, I. P., Connor, C. B., and Plunkett, G.: A 7000 yr perspective on volcanic ash clouds affecting northern Europe, *Geology*, 39, 887–890, doi:10.1130/G32146.1, 2011. 74

25 Tesche, M., Glantz, P., Johansson, C., Norman, M., Hiesch, A., Ansmann, A., Althausen, D., Engelmann, R., and Seifert, P.: Volcanic ash over Scandinavia originating from the Grimsvotn eruptions in May 2011, *J. Geophys. Res.-Atmos.*, 117, D09201, doi:10.1029/2011JD017090, 2012. 107

Thorarinsson, S.: Greetings from Iceland: ash-falls and volcanic aerosols in Scandinavia, *Geogr. Ann. A*, 63, 109–118, 1981. 107

30 Turnbull, K., Johnson, B., Marenco, F., Haywood, J., Minikin, A., Weinzierl, B., Schlager, H., Schumann, U., Leadbetter, S., and Woolley, A.: A case study of observations of volcanic ash from the Eyjafjallajökull eruption: 1. In situ airborne observations, *J. Geophys. Res.-Atmos.*, 117, D00U12, doi:10.1029/2011JD016688, 2012. 81

Big grains go far

J. A. Stevenson et al.

Title Page

Abstract

Introduction

Conclusions

References

Tables

Figures



Back

Close

Full Screen / Esc

Printer-friendly Version

Interactive Discussion



- Wastegård, S., Wohlfarth, B., Subetto, D. A., and Sapelko, T. V.: Extending the known distribution of the Younger Dryas Vedde Ash into northwestern Russia, *J. Quaternary Sci.*, 15, 581–586, doi:10.1002/1099-1417(200009)15:6<581::AID-JQS558>3.0.CO;2-3, 2000. 104
- Webster, H. N., Thomson, D. J., Johnson, B. T., Heard, I. P. C., Turnbull, K., Marengo, F., Kristiansen, N. I., Dorsey, J., Minikin, A., Weinzierl, B., Schumann, U., Sparks, R. S. J., Loughlin, S. C., Hort, M. C., Leadbetter, S. J., Devenish, B. J., Manning, A. J., Witham, C. S., Haywood, J. M., and Golding, B. W.: Operational prediction of ash concentrations in the distal volcanic cloud from the 2010 Eyjafjallajökull eruption, *J. Geophys. Res.-Atmos.*, 117, D00U08, doi:10.1029/2011JD016790, 2012. 87, 88
- Wen, S. and Rose, W. I.: Retrieval of sizes and total masses of particles in volcanic clouds using AVHRR bands 4 and 5, *J. Geophys. Res.*, 99, 5421–5431, doi:10.1029/93JD03340, 1994. 69, 70, 71, 82, 115
- White, J. and Houghton, B.: Primary volcanoclastic rocks, *Geology*, 34, 677–680, doi:10.1130/G22346.1, 2006. 67
- Wohletz, K., Sheridan, M., and Brown, W.: Particle size distributions and the sequential fragmentation/transport theory applied to volcanic ash, *J. Geophys. Res.*, 94, 15703–15721, 1989. 76
- Zdanowicz, C. M., Zielinski, G. A., and Germani, M. S.: Mount Mazama eruption: calendrical age verified and atmospheric impact assessed, *Geology*, 27, 621–624, doi:10.1130/0091-7613(1999)027<0621:MMECAV>2.3.CO;2, 1999. 104
- Zielinski, G. A., Mayewski, P. A., Meeker, L. D., Grönvold, K., Germani, M. S., Whitlow, S., Twickler, M. S., and Taylor, K.: Volcanic aerosol records and tephrochronology of the Summit, Greenland, ice cores, *J. Geophys. Res.*, 102, 26625–26640, doi:10.1029/96JC03547, 1997. 104

Table 1. Grainsize data for distal ash deposition. Distal grainsize measurements are not routinely reported in tephra literature, but published examples demonstrate that distal tephra deposits are dominated by grains 30–80 μm , with maximum lengths often greater than 100 μm . Grainsizes are long axis measurements made by optical or scanning electron microscopy, except^a, which were obtained by laser particle size analysis. GRIP, NGRIP, GISP and GISP2 are locations of ice cores in Greenland. The largest eruptions, with Volcano Explosivity Index (VEI) scores of 7 or 8, are rare (recurrence intervals of > 1000 and > 10 000 years, respectively; Newhall and Self, 1982).

Eruption	Deposit location	Distance (km)	Grainsize (μm)	Notes	Reference
Chaiten, Chile, 2008	E Argentina	550	20–40 (mode)	Little change in mean from 300 km	Durant et al. (2012)
Hudson, Chile, 1991	E Argentina	550	~ 32 (mode)	Maximum 125–250 μm	Scasso et al. (1994)
Mt St Helens, USA, 1980	NW USA	630	38% 32–125	64–125 μm is 10–15% at 260–630 km	Durant et al. (2009)
Mt Berlin, Antarctica	Siple Dome	675	20–30	Some 50 μm , 24 layers in 120 ka	Dunbar and Kurbatov (2011)
Taupo Whakamaru	Chatham Island	864	75 (mode) ^a	34% > 63 μm ; 1500 km ³ erupted; VEI 8	Matthews et al. (2012)
Vedde Ash, Katla?	Skye, Scotland	975	24–150 ^b	Basalt and rhyolite	Davies et al. (2001)
Hekla 1510	Scotland	860–1030	< 70 ^b		Dugmore et al. (1996)
Grímsvötn 2011	Scotland	1000	20–80 ^b	Collected in rainwater	Stevenson et al. (2013)
Eyjafjallajökull 2010	UK	1000–1500	25–100	Collected in rainwater	Stevenson et al. (2012)
Jan Mayen	NGRIP	1200	40–75 ^b		Abbott et al. (2012)
Bruneau-Jarbridge, Miocene?	Nebraska	1200	77 ^a (mode)	Some grains > 250 μm ; 0.4–2 m thick beds	Riley et al. (2003)
Saksunarvatn, Grímsvötn	NGRIP	1500	< 150 ^b	Brown, cusped	Mortensen et al. (2005)
LY1877, Papua New Guinea?	Lynch's Crater, Australia	> 1500	40–60	thin-walled vesicular rhyolite	Coulter et al. (2009)
Many Iceland	NGRIP	> 1500	> 30 ^b	Up to 80 μm , some form visible layer	Abbott et al. (2012)
Many Iceland	GRIP	> 1500	> 30 ^b	Up to 80 μm	Abbott et al. (2012)
Vedde Ash, Katla?	NGRIP	1550	< 70 ^b	Platy, cusped, bubble walls	Mortensen et al. (2005)
Many Iceland	W Sweden	1600	20–60 ^b	Dominated by rhyolite composition	Bergman et al. (2004)
Saksunarvatn, Grímsvötn	NW Germany	2000	< 110 ^b	Colourless and brown	Bramham-Law et al. (2013)
Campanian Ignimbrite, Italy	Various	880–2300	Median 41–50 ^a	95th percentile 147–212 ^a ; VEI 7	Engwell et al. (2013)
Vedde Ash, Katla?	SW Germany	2400	> 10	Min diameter is electron beam size	Blockley et al. (2007)
Saksunarvatn, Grímsvötn	SW Poland	2400	20–60 ^b	Platy, curvilinear	Housley et al. (2013)
Vedde Ash, Katla?	NW Russia	2450	> 24 ^a	Layer is 2–3 mm thick in Norway	Wastegård et al. (2000)
Vedde Ash, Katla?	Switzerland	2500	> 10	Min diameter is electron beam size	Blockley et al. (2007)
Vedde Ash, Katla?	Italy	2650	> 10	Min diameter is electron beam size	Lane et al. (2011)
Toba YTT	Jwalapuram, India	2669	53 ^a (mode)	10% > 63 μm ; 2500 km ³ erupted; VEI 8	Matthews et al. (2012)
Vedde Ash, Katla?	Slovenia	2800	30–100 ^b	Platy, curvilinear	Lane et al. (2011)
Katmai, Alaska, 1912	NGRIP	4426	–		Coulter et al. (2012)
Mazama 7675 \pm 150 b2k	GISP	5300	< 20	VEI 7	Zdanowicz et al. (1999)
Multiple	Dome C, Antarctica	> 6000	~ 10	Geochemistry unlike local sources	De Angelis et al. (1985)
Cascades and Alaska	Newfoundland	5000–7000	30–40	Rhyolite. Fluted, vesicular, platy	Pyne-O'Donnell et al. (2012)
El Chichón, Mexico, 1982	GISP2	6450	< 10	Collected in snow	Zielinski et al. (1997)
Samalás 1257	GISP2	13 500	< 5	Also found at South Pole	Palais et al. (1992); Lavigne et al. (2013)

^b indicate data used in Fig. 12.

[Title Page](#)
[Abstract](#)
[Introduction](#)
[Conclusions](#)
[References](#)
[Tables](#)
[Figures](#)
[Back](#)
[Close](#)
[Full Screen / Esc](#)
[Printer-friendly Version](#)
[Interactive Discussion](#)


Big grains go far

J. A. Stevenson et al.

Title Page

Abstract

Introduction

Conclusions

References

Tables

Figures

◀

▶

◀

▶

Back

Close

Full Screen / Esc

Printer-friendly Version

Interactive Discussion



Table 2. Grainsize distribution parameters for distal cryptotephra. D_{50N} is the median number diameter (μm), σ is the geometric standard deviation of the lognormal number distribution of grain length, except for two Eyjafjallajökull 2010 and Askja 1875 laser particle sizer examples, which are better fitted by a Weibull distribution of particle volume. The Weibull scale and shape parameters are given in this case (italics). Data from Persson (1971) are also summarised. 95% of the particles have length of less than D_{95N} (μm).

Eruption	Location	Distance (km)	Method	D_{50N}	σ	D_{95N}
Hekla 4	Shetland	1050	Microscope	55.41	1.49	106.8
Hekla 4	Malham	1050	Microscope	47.89	1.46	89.2
Hekla Selsund	Shetland	1050	Microscope	69.19	1.43	124.6
Hekla 1104	Shetland	1050	Microscope	54.09	1.47	101.9
Hekla 1158	Shetland	1050	Microscope	47.49	1.40	82.6
Hekla 1947	Fallahogy	1250	Microscope	48.70	1.55	100.1
Glen Garry	Malham	1450	Microscope	53.34	1.47	100.5
Grímsvötn 2011	Armagh	1250	Microscope	22.09	1.66	50.8
Grímsvötn 2011	Auldearn 23 May	980	Microscope	22.82	1.57	47.9
Grímsvötn 2011	Auldearn 24 May	1050	Microscope	22.57	1.56	46.9
Grímsvötn 2011	Lerwick	960	Microscope	19.92	1.58	42.3
Eyjafjallajökull 2010	Aberdeen	1200	Microscope	29.9	1.63	67.0
Eyjafjallajökull 2010	Benbecula	955	Microscope	17.1	1.39	29.4
Eyjafjallajökull 2010	Leicestershire	1610	Microscope	26.2	1.38	44.7
Persson (various)	Scandinavia	650–1840	Microscope	19–33	1.43–1.98	45–100
Eyjafjallajökull 2010	Faroe Islands	675	Coulter	40.66 ^a	1.37 ^b	90.6
Askja 1875	Trysil, Norway	1500	Coulter	55.07 ^a	1.48 ^b	115.5

^a Weibull scale; ^b Weibull shape.

Big grains go far

J. A. Stevenson et al.

Title Page

Abstract

Introduction

Conclusions

References

Tables

Figures

◀

▶

◀

▶

Back

Close

Full Screen / Esc

Printer-friendly Version

Interactive Discussion



Table 3. Estimated grainsize mass distribution parameters for distal cryptotephra using data from Table 2 and extreme examples of ratios of particle length to particle spherical equivalent diameter from Riley et al. (2003). D_{50M} is the median mass diameter (μm); 95 % of the mass is within particles with diameters less than D_{95M} (μm).

Eruption	Location	Basalt (1.05)		Rhyolite (1.33)	
		D_{50M}	D_{95M}	D_{50M}	D_{95M}
Hekla 4	Shetland	85.03	163.85	67.13	129.36
Hekla 4	Malham	70.09	130.61	55.33	103.11
Hekla Selsund	Shetland	96.72	174.20	76.36	137.52
Glen Garry	Malham	79.30	149.44	62.60	117.98
Hekla 1104	Shetland	80.41	151.54	63.48	119.64
Hekla 1158	Shetland	63.52	110.48	50.15	87.22
Hekla 1947	Fallahogy	82.52	169.69	65.15	133.96
Grímsvötn 2011	Armagh	45.46	104.64	35.89	82.61
Grímsvötn 2011	Auldearn 23 May	40.02	84.03	31.59	66.34
Grímsvötn 2011	Auldearn 24 May	38.90	80.84	30.71	63.82
Grímsvötn 2011	Lerwick	35.54	75.42	28.06	59.54

Big grains go far

J. A. Stevenson et al.

Title Page

Abstract

Introduction

Conclusions

References

Tables

Figures



Back

Close

Full Screen / Esc

Printer-friendly Version

Interactive Discussion



Table 4. Calculated minimum mean wind speeds transporting ash from Icelandic eruptions across Europe, based on observations. It is assumed that the start time was the onset of eruption and that the plume travelled by the most direct route to the location, as the crow flies. Where PM_{10} is given, time is from eruption onset to observed peak PM_{10} measurement.

Eruption	Time + Date of Eruption	Location of Observation	Time + Date of Observation	Travel Dist. (km)	Travel Time (hrs)	Mean Wind Speed (ms^{-1})	Ref.
Hekla 1947	06:40 UTC 29 Mar 1974	Helsinki (Finland)	11:00 UTC 31 Mar 1947	2292	51	12	Thorarinsson (1981)
Eyjafjallajökull 2010	09:00 UTC 14 Apr 2010	Mulhouse (France) PM_{10}	03:00 UTC 18 Apr 2010	2396	90	7	Colette et al. (2011)
Eyjafjallajökull 2010	09:00 UTC 14 Apr 2010	Budapest (Hungary) PM_{10}	00:15 UTC 18 Apr 2010	2950	87	9	Stevenson et al. (2012)
Grimsvotn 2011	19:00 UTC 21 May 2011	Aberdeen (UK) PM_{10}	01:00 UTC 24 May 2011	1856	55	9	Stevenson et al. (2013)
Grimsvotn 2011	19:00 UTC 21 May 2011	Birkenes (Norway) PM_{10}	12:00 UTC 24 May 2011	1507	65	6	Tesche et al. (2012)
Grimsvotn 2011	19:00 UTC 21 May 2011	Goethenburg (Sweden) PM_{10}	12:00 UTC 24 May 2011	1725	65	7	Tesche et al. (2012)
Grimsvotn 2011	19:00 UTC 21 May 2011	Stockholm (Sweden) PM_{10}	00:00 UTC 25 May 2011	1935	77	7	Tesche et al. (2012)
Askja 1875	05:30 UTC 29 Mar 1875	Bergen (Norway)	22:00 UTC 29 Mar 1875	1118	16.5	19	Thorarinsson (1981)
Askja 1875	05:30 UTC 29 Mar 1875	Trysil (Norway)	04:30 UTC 30 Mar 1875	1488	23	18	Thorarinsson (1981)
Askja 1875	05:30 UTC 29 Mar 1875	Stockholm (Sweden)	12:00 UTC 30 Mar 1875	1896	30.5	17	Thorarinsson (1981)

Big grains go far

J. A. Stevenson et al.

Title Page

Abstract

Introduction

Conclusions

References

Tables

Figures



Back

Close

Full Screen / Esc

Printer-friendly Version

Interactive Discussion

**Table 5.** Summary of transport model results. Ash Hollow results are based on particles of rhyolite composition.

Scheme	Maximum diameter airborne for 24 h (μm)	Maximum diameter reaching London (μm)
Stokes'	41	29
Ganser	50	33
Ash Hollow (Equiv.Diam)	80	60
Ash Hollow (Length)	115–135	85–105

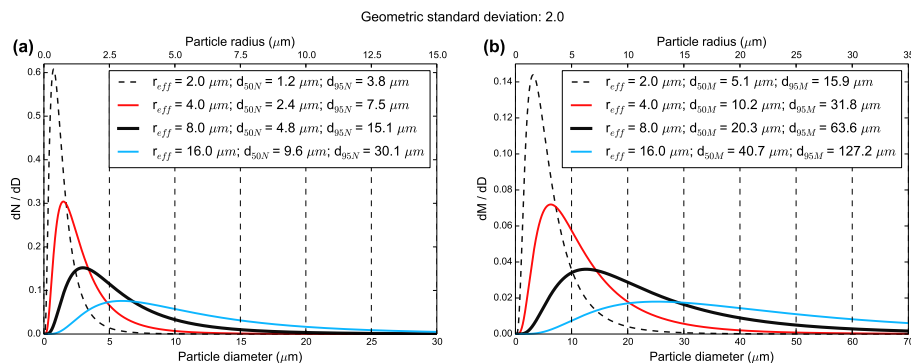


Figure 1. Lognormal number, **(a)**, and mass, **(b)**, grain size distributions corresponding to different effective radii, with a geometric standard deviation of 2.0. The mass distribution is shifted towards coarser values compared to the number distribution. These calculations assume that particles are dense spheres. As a convenient rule-of-thumb, the mass median diameter and mass 95th percentile diameter are approximately $2.5\times$ and $8\times r_{\text{eff}}$. For $r_{\text{eff}} > 8 \mu\text{m}$, more than half of the mass of the distribution is contained in cryptotephra-sized particles ($> 20 \mu\text{m}$), but only distributions with larger r_{eff} contain significant proportions of the coarsest cryptotephra-sized particles (i.e. $> 100 \mu\text{m}$). If the geometric standard deviation is less than 2.0, the size of the coarsest particles is much reduced.

[Title Page](#)
[Abstract](#)
[Introduction](#)
[Conclusions](#)
[References](#)
[Tables](#)
[Figures](#)

[Back](#)
[Close](#)
[Full Screen / Esc](#)
[Printer-friendly Version](#)
[Interactive Discussion](#)

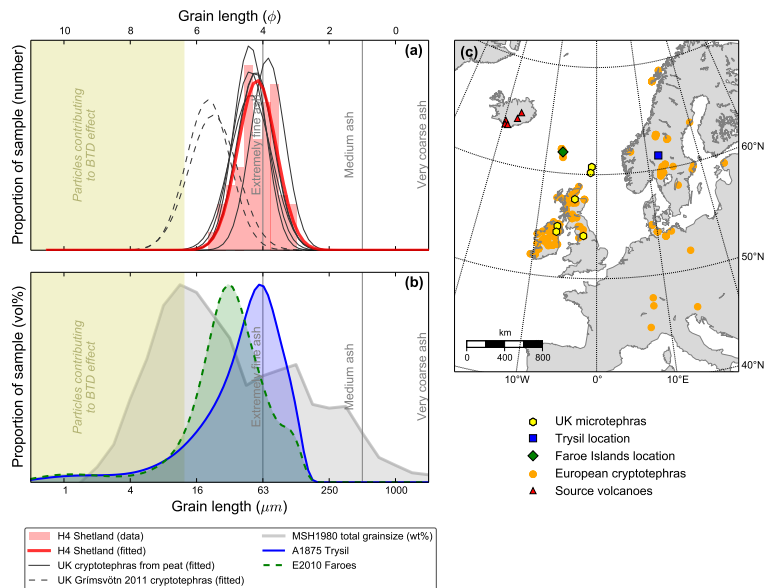



Figure 2. Deposition of Icelandic ash in Europe. **(a)** Long axis number distributions of UK cryptotephra. The example histogram and red fitted curve represent the Hekla 4 eruption collected in Shetland, Scotland. The fitted curves (lognormal distribution) of UK cryptotephras extracted from peat or collected during the Grímsvötn 2011 eruption are also plotted. Grain-sizes measured in ϕ units, where $\phi = -\log_2(d \text{ mm})$ are used in volcanology and sedimentology. **(b)** Particle size distributions measured by laser diffraction particle size analysis for two distal Icelandic cryptotephras. Particles $< 12 \mu\text{m}$ are present only as a minor component and the modal grainsizes are similar to **(a)**. The total deposit grainsize distribution of the 1980 Mt St Helens eruption is plotted for comparison and demonstrates the wide range of particle sizes erupted during explosive rhyolite eruptions (Carey and Sigurdsson, 1982). **(c)** Map of sample locations and source volcanoes. Other European cryptotephras are plotted for context (Lawson et al., 2012; Lane et al., 2012; Bramham-Law et al., 2013; Housley et al., 2013). Limitations of identification methods imply that they have a minimum grainsize of $\sim 20 \mu\text{m}$.

Big grains go far

J. A. Stevenson et al.

Title Page

Abstract

Introduction

Conclusions

References

Tables

Figures



Back

Close

Full Screen / Esc

Printer-friendly Version

Interactive Discussion

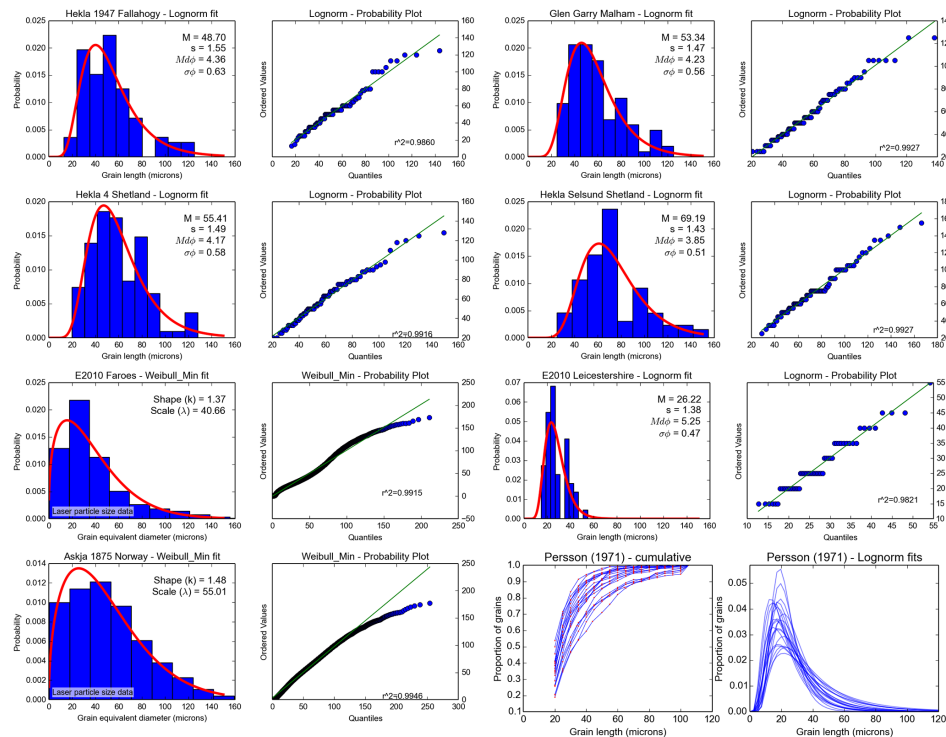


Figure 3. Statistical model fits to distal tephra grainsize distributions. Optical microscope cryptotephra lengths are well-characterised by a lognormal distribution. Coulter counter data (Askja 1875 Norway, Eyjafjallajökull 2010 Faroes), which have a fine tail, are better fit by Weibull distributions than normal or lognormal, but the model overestimates the proportions of the coarsest particles. Data from Persson (1971) are shown for comparison. See Supplement for additional examples.

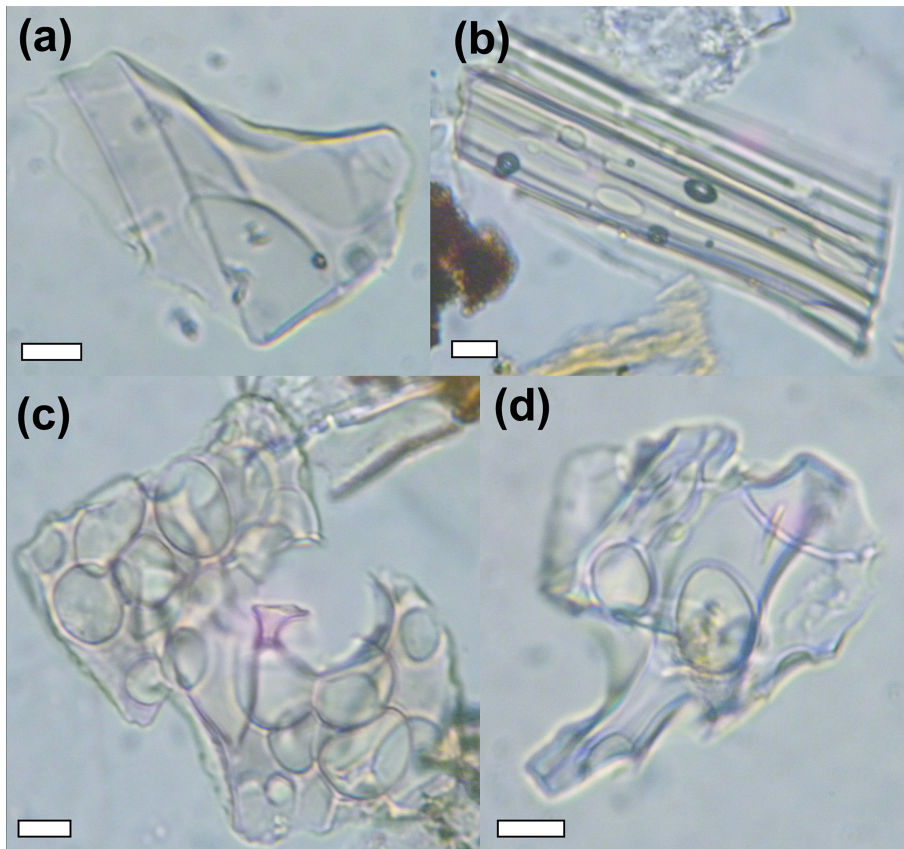


Figure 4. Light microscope images illustrating tephra shards found in Europe: **(a and d)** Glen Garry tephra, N. England; **(b and c)** Hekla-Selsund tephra, Shetland Isles. The tephra shards have different morphological characteristics: **(a)** platy; **(b)** pulled; **(c)** bubbly; **(d)** bubbly and platy. Their optical and aerodynamic properties are unlike dense spheres. Scale bars are 10 μm in length.

Title Page

Abstract

Introduction

Conclusions

References

Tables

Figures

◀

▶

◀

▶

Back

Close

Full Screen / Esc

Printer-friendly Version

Interactive Discussion



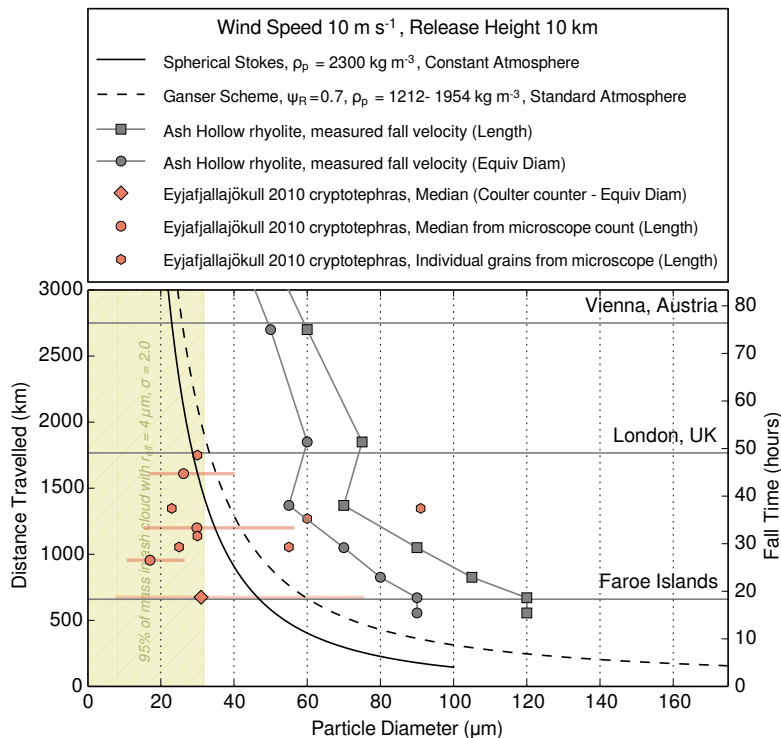


Figure 6. Modelled travel distance of ash particles as a function of particle diameter. Travel distances are calculated using Stokes' Law (for particles up to 100 μm diameter), the Ganser scheme and the measured fall velocities of Ash Hollow rhyolite grains (in terms of both length and equivalent area diameter; Riley et al., 2003). The grey horizontal lines represent the distances from Eyjafjallajökull to various European locations. Measured particle sizes from the Eyjafjallajökull 2010 eruption are plotted for comparison. Horizontal coloured bars extend from the 10th to the 90th percentiles of the PSDs. The shaded region indicates the 95th percentile size range implied by an r_{eff} of 4 μm and σ of 2.0.

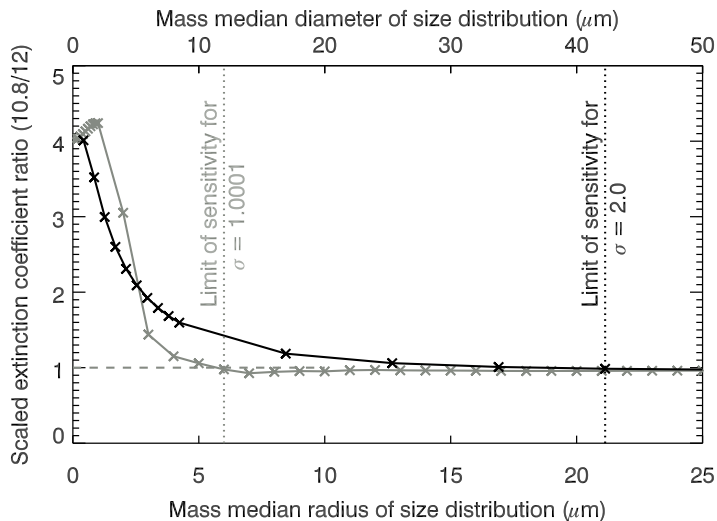


Figure 7. Scaled extinction coefficient ratio for SEVIRI channels at 10.8 and 12.0 μm for spherical andesite volcanic ash particles as a function of ash particle size. Mie calculations were performed to calculate the absorption and scattering properties; these were combined to form a scaled extinction coefficient. This is an approximation for the effects of multiple scattering and therefore a better indication of the extinction properties than the single-scattering extinction coefficient. The geometric standard deviation (σ) was set to 1.0001 to effectively create an infinitely narrow distribution where all the particles are a single size (grey line), and the mass median radius (r_m) of the size distribution was varied from 0.1 to 25 μm . The dotted line shows the grainsize at which the reverse absorption technique becomes insensitive to andesite volcanic ash. It is not possible to use BTM effects to identify or automatically detect uniformly-sized spherical andesite particles with radius $> 6 \mu\text{m}$. A real ash cloud contains a range of particle sizes. With a geometric standard deviation of 2.0, the BTM effect extends to mass median radius of 21 μm (black line). This corresponds to an effective radius of 16.5 μm , which is comparable findings of Wen and Rose (1994). The sensitivity decreases rapidly with increasing mass median radius, particularly below the single particle detection limit of 6 μm .

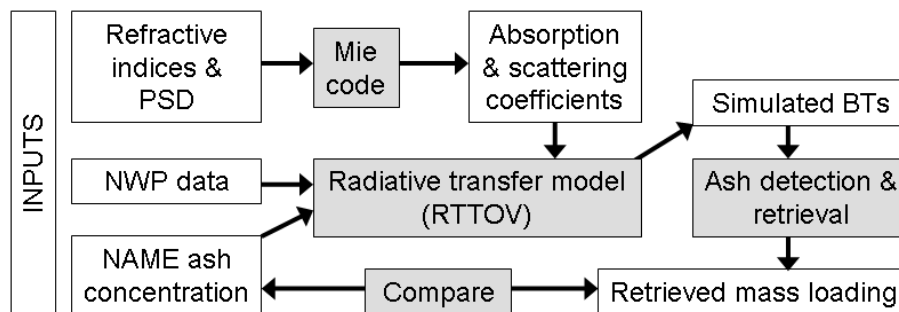


Figure 8. Schematic of the method used to compare input ash mass concentration and retrieved ash mass loading. The white boxes contain data and the grey boxes represent code.

[Title Page](#)[Abstract](#)[Introduction](#)[Conclusions](#)[References](#)[Tables](#)[Figures](#)[◀](#)[▶](#)[◀](#)[▶](#)[Back](#)[Close](#)[Full Screen / Esc](#)[Printer-friendly Version](#)[Interactive Discussion](#)

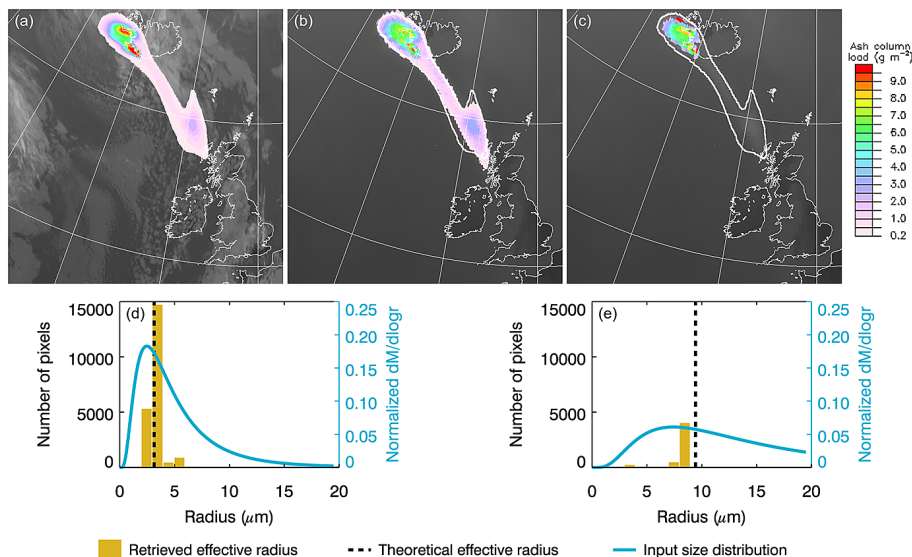


Figure 9. Ash mass loading and effective radius data for 12:00 UTC on 14 May 2010. **(a)** NAME ash column mass loading overlaid on the SEVIRI 10.8 μm BT image for the corresponding time. **(b)** and **(c)** are retrieved ash column mass loading data from simulated SEVIRI infrared data using a lognormal PSD with geometric standard deviation of 2.0 and a mass median radius of 4 and 12 μm respectively. The light grey line in **(b)** and **(c)** shows the extent of the NAME ash coverage (where mass loading > 0.2 g m⁻²); this is overlaid on a simulated 10.8 μm infrared image (simulated without clouds). Slightly cooler temperatures indicate the presence of volcanic ash within the zone of NAME ash coverage, which may be identified by a skilled forecaster. **(d)** and **(e)** are histograms of retrieved effective radii from the same simulated SEVIRI data as **(b)** and **(c)** respectively. The blue curves in **(d)** and **(e)** show the input mass PSD, while the dotted line shows the corresponding theoretical effective radius.

Big grains go far

J. A. Stevenson et al.

Title Page

Abstract

Introduction

Conclusions

References

Tables

Figures



Back

Close

Full Screen / Esc

Printer-friendly Version

Interactive Discussion

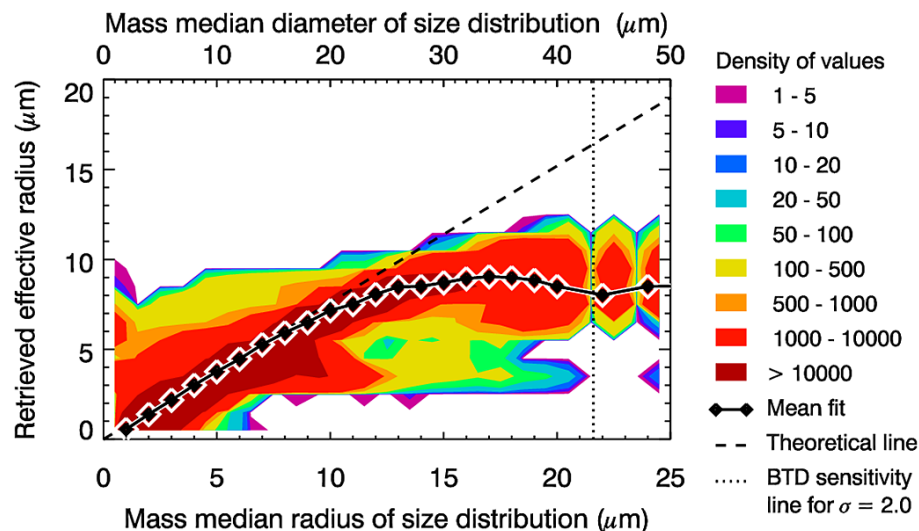


Figure 10. Retrieved effective radius for pixels with low uncertainty (i.e. total cost < 12) and mass loading $> 0.2 \text{ g m}^{-2}$ against mass median radius of a lognormal PSD with geometric standard deviation of 2.0. The coloured contours represent the density of values from the pixels in the 12 cases described above. The black diamonds are the mean retrieved effective radius for the given mass median radius of the PSD, which tracks the theoretical effective radius up to around $10 \mu\text{m}$. PSDs that are coarser than this still return a mean effective radius of around $9 \mu\text{m}$. The vertical dotted line shows the limit of sensitivity for the BTD method; ash-containing pixels in coarser PSDs were identified by additional tests.

Title Page

Abstract

Introduction

Conclusions

References

Tables

Figures

◀

▶

◀

▶

Back

Close

Full Screen / Esc

Printer-friendly Version

Interactive Discussion

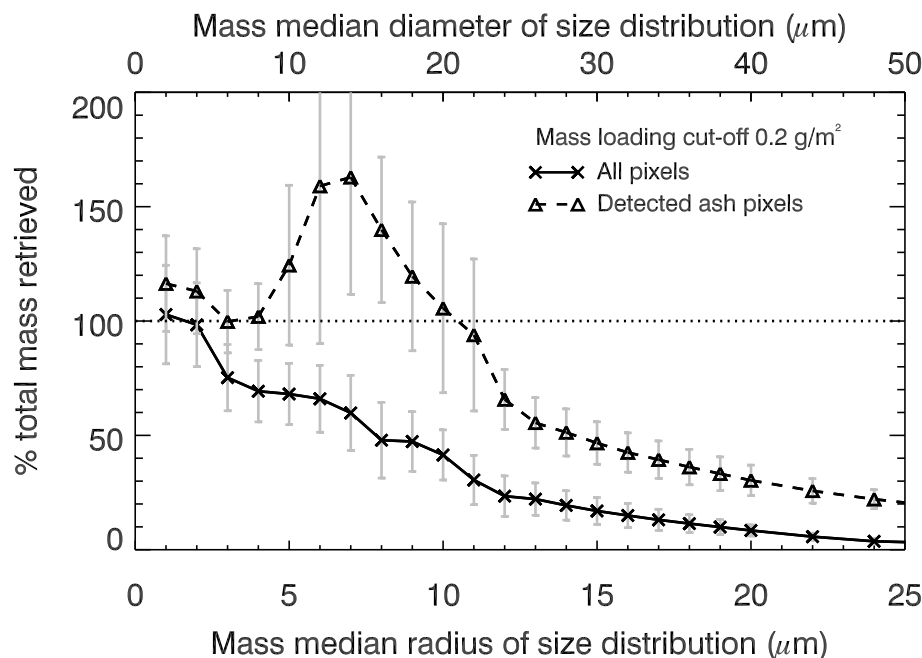


Figure 11. Retrieved mass loading for pixels with low uncertainty (i.e. total cost < 12) against mass median radius of a lognormal PSD with a geometric standard deviation of 2.0. Data from all 12 cases are combined. Percentage of total mass retrieved is the sum of the retrieved total column loadings \times area, divided by the total mass input into the simulated imagery from the NAME model. The dashed line includes only those for which volcanic ash was detected in the simulated imagery; the solid line includes all pixels that contained ash in the input NAME data. The error bars show the standard deviation of the data.

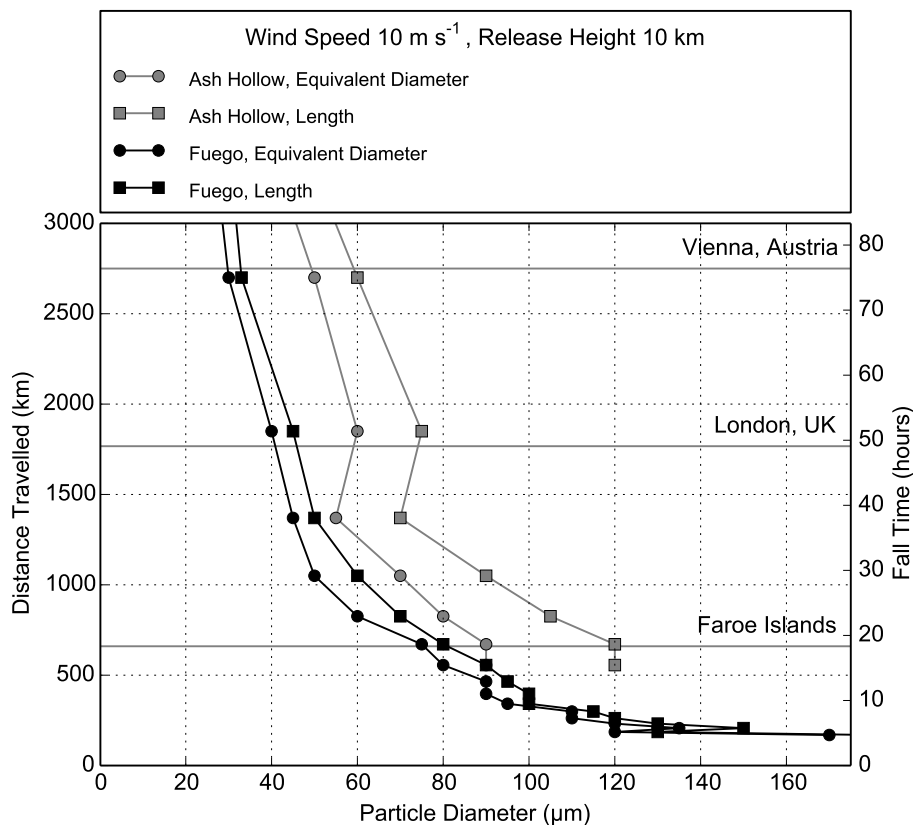


Figure 12. The effect of composition on cryptotephra range. Travel distance and travel time of Fuego (basaltic) and Ash Hollow (rhyolitic) ash particles using their measured fall velocities at sea level (Riley et al., 2003), where particle diameter is taken to be equivalent area diameter and long axis length. The grey horizontal lines represent the distances from Eyjafjallajökull to various European locations. Rhyolite grains travel further than basaltic grains.